nuclear fusion
IAEA

PAPER

# First principle-based multi-channel integrated modelling in support of the design of the Divertor Tokamak Test facility

To cite this article: I. Casiraghi *et al* 2021 *Nucl. Fusion* **61** 116068

IOP Publishing | International Atomic Energy Agency Nuclear Fusion

Nucl. Fusion **61** (2021) 116068 (21pp) https://doi.org/10.1088/1741-4326/ac21b9

# First principle-based multi-channel integrated modelling in support of the design of the Divertor Tokamak Test facility

**I. Casiraghi[1,2,*], P. Mantica[2], F. Koechl[3], R. Ambrosino[4,5,6], B. Baiocchi[2], A. Castaldo[5], J. Citrin[7,8], M. Dicorato[1], L. Frassinetti[9], A. Mariani[1,2], P. Vincenzi[10], P. Agostinetti[10], L. Aucone[11], L. Balbinot[10,12], S. Ceccuzzi[6,13], L. Figini[2], G. Granucci[2], P. Innocente[10], T. Johnson[9], H. Nyström[9] and M. Valisa[10]**

[1] Dipartimento di Fisica 'G. Occhialini', Università di Milano-Bicocca, Milan, Italy
[2] Istituto per la Scienza e Tecnologia dei Plasmi, CNR, Milan, Italy
[3] CCFE, Culham Science Centre, Abingdon, United Kingdom
[4] Università degli Studi di Napoli Federico II, Naples, Italy
[5] Consorzio CREATE, Naples, Italy
[6] DTT S.C. a r.l., Frascati, Italy
[7] DIFFER—Dutch Institute for Fundamental Energy Research, Eindhoven, Netherlands
[8] Science and Technology of Nuclear Fusion Group, Eindhoven University of Technology, Eindhoven, Netherlands
[9] Fusion Plasma Physics, ECSS, KTH Royal Institute of Technology, Stockholm, Sweden
[10] Consorzio RFX (CNR, ENEA, INFN, Università di Padova, Acciaierie Venete SpA), Padua, Italy
[11] Politecnico di Milano, Milan, Italy
[12] Università degli Studi di Padova, Padua, Italy
[13] ENEA C.R.Frascati, Frascati, Italy

E-mail: i.casiraghi3@campus.unimib.it

Received 28 May 2021, revised 25 July 2021
Accepted for publication 26 August 2021
Published 14 October 2021

**Abstract**

An intensive integrated modelling work of the main scenarios of the new Divertor Tokamak Test (DTT) facility with a single null divertor configuration has been performed using first principle quasi-linear transport models, in support of the design of the device and of the definition of its scientific work programme. First results of this integrated modelling work on DTT ($R_0 = 2.14$ m, $a = 0.65$ m) are presented here along with outcome of the gyrokinetic simulations used to validate the reduced models in the DTT range of parameters. As a result of this work, the heating mix has been defined, the size of device has been increased to $R_0 = 2.19$ m and $a = 0.70$ m, the use of pellets for fuelling has been recommended and reference profiles for diagnostic design, estimates of neutron yields and fast particle losses have been made available.

Keywords: divertor tokamak test facility, integrated modelling, quasi-linear transport models

(Some figures may appear in colour only in the online journal)

* Author to whom any correspondence should be addressed.

 

## 1. Introduction

Studying the controlled power and particle exhaust from a fusion reactor is a central research topic of the European Fusion Roadmap [1, 2].

The International Thermonuclear Experimental Reactor (ITER) [3] is planned to test a conventional metal divertor operating in fully detached plasma conditions. This baseline approach to the power exhaust problem may be unsuitable for extrapolation to the operating conditions of the DEMOnstration power plant (DEMO) [4] and future reactors, requiring plasma-facing components able to cope with huge power fluxes in the range of 10–20 MW m$^{-2}$. Therefore, studying and developing an alternative exhaust strategy is crucial to mitigate this risk.

This is the main task of the new Divertor Tokamak Test (DTT) facility [5–7], whose construction will shortly begin in Frascati, Italy, with the first plasma planned for 2026. The DTT design is advanced but will be kept flexible with regard to the choice of the divertor until 2023, when the outcome of the work conducted under the EUROfusion PEX ad hoc group will be available to drive the best choice for the divertor.

For the optimisation of various aspects of the DTT design, it is of key importance to perform integrated modelling of foreseen operational scenarios using first principle-based transport models and state-of-the-art modules for heating, fuelling and magnetic equilibrium. Integrated modelling allows us to predict the main plasma profiles as a result of non-linear interactions between plasma, heating and fuelling, and impurity influxes, as well as amongst different transport channels.

The aim of this paper, which reports the first DTT simulations using theory-based transport models, is to support DTT design, specifically the definition of the heating mix, the design of the neutron shields, the assessment of fast particle losses and the design of diagnostic systems, as well as to help in the elaboration of a scientific work programme for DDT.

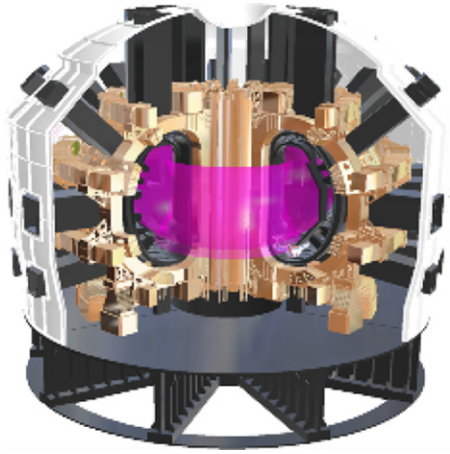

**Figure 1.** DTT device.

**Table 1.** Main parameter comparison between the DTT configuration simulated in this paper and future ITER and EU DEMO devices [10–12].

| | DTT | ITER | EU DEMO |
|---|---|---|---|
| $R$ (m) | 2.14 | 6.2 | 9.1 |
| $a$ (m) | 0.65 | 2.0 | 2.93 |
| $A$ | 3.3 | 3.1 | 3.1 |
| $I_{pl}$ (MA) | 5.5 | 15 | 19.6 |
| $B_t$ (T) | 6 | 5.3 | 5.7 |
| $P_{tot}$ (MW) | 45 | 150 | 460 |
| $P_{sep}$ (MW) | 32 | 87 | 154 |
| $P_{sep}/R$ (MW m$^{-1}$) | 15 | 14 | 17 |
| $\lambda_q$ (mm) | 0.7 | 0.9 | 1.0 |
| Pulse length (s) | 100 | 400 | 7600 |
| $\beta_N$ (%) | 1.6 | 1.6 | 2.6 |
| $\nu_e^*$ at $r/a = 0.5$ ($10^{-2}$) | 1.1 | 1.1 | 0.5 |
| $\rho^*$ ($10^{-3}$) | 3.3 | 2.0 | 1.5 |
| $\langle n \rangle$ ($10^{20}$ m$^{-3}$) | 1.8 | 1.0 | 0.9 |
| $\langle T_e \rangle$ (keV) | 6.7 | 8.5 | 13 |
| $\tau_E$ (s) | 0.4 | 3.6 | 4.2 |

## 2. The DTT project

The new DTT is a D-shaped superconducting device whose construction will shortly begin at the ENEA Research Center in Frascati, Italy. A drawing of the DTT device is shown in figure 1.

The characteristics of DTT were chosen to make it ITER and DEMO relevant, so that exhaust solutions could be extrapolated to reactor-grade plasma. Bearing in mind the requirement of strong compatibility with the operating conditions in DEMO, DTT is designed to be a bulk-edge-integrated experiment with a reactor relevant bulk. Therefore, the DTT dimensionless physical parameters should be as close as possible to those of ITER and DEMO. It is not possible to simultaneously preserve all these quantities, and hence DTT has been scaled down following the so called 'weak scaling' described in [8]. Since the $P_{sep}/R$ parameter, where $P_{sep}$ is the power exiting through the separatrix, is recognised as a key metric for the extent of the exhaust issue in a tokamak, geometry and auxiliary power coupled to the plasma have been chosen to guarantee a value of $P_{sep}/R = 15$ MW m$^{-1}$, similar to those foreseen for ITER and DEMO. Thus, the power at the divertor in DTT and DEMO will be comparable.

Table 1 shows rough indications for both the dimensional and dimensionless parameters of the DTT configuration simulated in this paper compared to ITER and EU DEMO.

The collisionality has been calculated as $\nu_e^* = 6.92 \times 10^{18}\ (qR_0 n_e Z_{eff} \ln \Lambda_e)\left(T_e^2 \varepsilon^{3/2}\right)$, where $n_e$ is expressed in m$^{-3}$, $T_e$ is expressed in eV, and $\varepsilon$ is the inverse aspect ratio [9].

The superconducting coils allow for a pulse length of up to 100 s, with plasma current $I_{pl} \leqslant 5.5$ MA and with toroidal field coils able to generate an on-axis toroidal magnetic field $B_t \leqslant 6$ T at $R = 2.14$ m. DTT has an up–down symmetric geometry, major radius $R_0 = 2.19$ m, minor radius $a = 0.70$ m, elongation $\kappa \leqslant 1.89$, and average triangularity $\langle \delta \rangle \leqslant 0.4$. The device size was recently increased from the previous values $R_0 = 2.14$ m, $a = 0.65$ m. The simulations reported here are for the 2.14 m device, and have contributed to the decision of its enlargement.

For the reference baseline DTT scenarios, a Greenwald density target value of $\langle n \rangle / n_G \sim 0.45$ (where $n_G$ is the Greenwald fraction defined in [13]), has been chosen in order to have a high operational flexibility, leaving open the possibility to explore higher densities in future scenarios.

The plasma shape parameters of the single null (SN) configuration are similar to those of the present European design of DEMO ($R_0/a \approx 3.1$, $\kappa_{95} \approx 1.55$–$1.8$, $\delta_{95} \approx 0.3$). The technical description of the DTT vacuum vessel, first wall and baseline divertor, and magnetic system is contained in [6].

To address the particle and power exhaust problem, alternative divertor solutions and improved plasma-facing materials will be developed and tested in DTT, thanks to its high flexibility in magnetic configuration and divertor choice. The various divertor solutions and technologies include liquid metal divertors, based on either capillary porous systems or boxes/pools systems, and advanced divertor configurations such as double null, quasi-snowflake, and SN with negative triangularity scenarios. The reference configuration that we will use in this paper is the SN.

DTT will be equipped with three auxiliary heating systems: a negative ion-based neutral beam injection system, a 60–90 MHz ion cyclotron resonance heating (ICRH) system, and a 170 GHz electron cyclotron resonance heating (ECRH) system.

In order to match the ITER and DEMO values of $P_{SEP}/R$, where $P_{SEP}$ is the power flowing through the last closed magnetic surface, a large amount of auxiliary power is needed (~45 MW in the full power (FP) scenario). The three heating systems will be progressively realised and installed on DTT.

The first experimental plasma (day-0 scenario) will be achieved using only 8 MW from the second harmonic ECRH (~7.2 MW at the plasma) at the half field operational point (plasma current $I_{pl} = 2$ MA and toroidal magnetic field $B_t = 3$ T). In a few years, the power coupled to the plasma will be increased up to ~25 MW in the phase called day-1 scenario, working at $I_{pl} = 4$ MA and $B_t = 5.85$ T. The heating mix in this initial phase has been fixed: 16 MW from ECRH (~14.4 MW at plasma), 4 MW from ICRH (~3 MW at plasma), and 7.0–7.5 MW at plasma from an NBI (at 400 keV). On the other hand, the definitive power mix for the DTT full performance scenario has been rediscussed with respect to the original options proposed in [6], following the simulation results reported in this paper, and new options have been evaluated, as discussed in section 3.6, within the following ranges of power at plasma: 26–36 MW of ECRH, 3–9 MW of ICRH, and 7.5–15 MW of NBI at energies between 200 and 600 keV.

The amount of heating power is an order of magnitude larger than typical power densities in present-day tokamaks and as foreseen in ITER. This trait, jointly with the cryogenic system needs, requires DTT to be an actively cooled device.

In addition to the main task dedicated to plasma exhaust, DTT will also be highly relevant for tokamak physics-integrated studies with reactor relevant parameters. Thanks to its high plasma core performance, DTT is located in a unique operational region, at high density but low collisionality, which is unexplored by present tokamaks (e.g. $n_e \sim (0.6$–$0.8) \times 10^{20}$ m$^{-3}$ and $\nu_e^* \approx (2.9 - 4.3) \times 10^{-2}$ at $r/a = 0.5$ in AUG high performance plasmas, $n_e \sim (0.7$–$0.9) \times 10^{20}$ m$^{-3}$ and $\nu_e^* \approx (2.2 - 3.9) \times 10^{-2}$ at $r/a = 0.5$ in JET-ILW baseline discharges).

Therefore, DTT will support the experimental program of ITER, operating in parallel with it, and it will address high-priority issues, such as ELM pacing, pellet fuelling, management and avoidance of disruptions, burning plasma energetic particle physics, and plasma control.

## 3. Integrated modelling of DTT single null scenarios

The integrated modelling of various DTT scenarios with the SN configuration in H-mode has been performed. These simulations solve the transport equations for heat, particle and momentum using a first principle transport model in a self-consistent magnetic equilibrium to predict steady-state radial profiles of the electron and ion temperatures, density (both main species and impurity), toroidal rotation, and current density. The heating profiles are also calculated consistently, as well as all non-linear interactions between heating and plasma and between the different transport channels.

As described in detail in section 3.2, integrated runs have been primarily done using the JINTRAC [14] suite of codes and in some cases using the ASTRA [15] transport solver with a mixed ASTRA–JINTRAC approach.

### 3.1. General settings

The performed simulations of DTT deuterium plasmas cover the region inside the separatrix. The equilibrium is calculated self-consistently during the run, keeping fixed the boundary, as described in section 3.3. Approximately 4 s of plasma evolution needs to be simulated until convergence, due to the current diffusion time.

The transport equations are solved within $\rho_{tor} = 0.94$, where $\rho_{tor} := \sqrt{\frac{(\Phi/\pi B_{tor})}{(\Phi/\pi B_{tor})_{max}}}$ is the normalised effective minor radius, i.e. the normalised radius that a magnetic surface with circular section should have in order to enclose the same toroidal magnetic flux $\Phi$. The values at the top of the edge pedestal are used as the boundary condition.

The pedestal pressure has been previously calculated using the Europed code [16] with the EPED1 model [17], which is based on two concepts. The pedestal transport is determined by turbulence driven by the kinetic ballooning modes (KBMs), which sets a soft boundary for the gradient. This is implemented in the code via the simple expression width $= 0.076 \times \sqrt{\beta_{pol}^{ped}}$, which provides one constraint that determines the gradient. However, once the pedestal reaches the KBM constraint, the pedestal height can still increase via the widening of the pedestal width. The widening continues until the peeling–ballooning (PB) modes are destabilised and an ELM is triggered. The EPED model determines pedestal height and pedestal width by identifying the intersection between the PB constraint and the KBM constraint.

The prescribed inputs of the Europed runs are the magnetic equilibrium, the electron density at the pedestal top $n_{\mathrm{epped}}$, the value of $\beta_{\mathrm{pol}}$, and the temperature and density at the separatrix $T_{\mathrm{e}}^{\mathrm{sep}}$ and the relative shift, defined as the distance between position of the pedestal density $n_{\mathrm{e}}^{\mathrm{pos}}$ and temperature $T_{\mathrm{e}}^{\mathrm{pos}}$ [18]. Note that the separatrix density $n_{\mathrm{e}}^{\mathrm{sep}}$ is not an input parameter, but is determined by $n_{\mathrm{e}}^{\mathrm{pos}} - T_{\mathrm{e}}^{\mathrm{pos}}$ and by the density offset applied in the SOL. For the same offset, the increase of the relative shift leads to the increase of $n_{\mathrm{e}}^{\mathrm{sep}}$ [19]. The value of $n_{\mathrm{e}}^{\mathrm{ped}}$ has been set to achieve a volume-averaged electron density $\langle n_{\mathrm{e}} \rangle \sim (0.40 - 0.47)\, n_{\mathrm{G}}$. $T_{\mathrm{i}} = T_{\mathrm{e}}$ has been assumed in the pedestal. Instead, the value of $\beta_{\mathrm{pol}}$ has been chosen, in an iterative way, in order to match the value predicted by the JINTRAC run. In the FP simulations, $n_{\mathrm{e}}^{\mathrm{ped}} = 1.4 \times 10^{20}\ \mathrm{m}^{-3}$, $\beta_{\mathrm{pol}} = 0.60$, a relative shift between $n_{\mathrm{e}}^{\mathrm{ped}}$ and $T_{\mathrm{e}}^{\mathrm{ped}}$ to obtain $n_{\mathrm{e}}^{\mathrm{sep}} \approx 0.25\, n_{\mathrm{e}}^{\mathrm{ped}}$, and $T_{\mathrm{e}}^{\mathrm{sep}} = 100$ eV values have been set and temperature values at the pedestal top of about $T_{\mathrm{e}}^{\mathrm{ped}} \simeq 2.4$ keV have been predicted. A more detailed discussion about the Europed input values is addressed in section 3.5.2.

Inside the top of the pedestal, the turbulent heat and particle transport is calculated by trapped-gyro-Landau-fluid (TGLF) [20–23], which is a gyrofluid and electromagnetic (EM) quasi-linear (QL) model with shaped flux surfaces, or by QuaLiKiz (QLK) [24, 25], which is a gyrokinetic and electrostatic QL transport model with circular flux surfaces. A large amount of work has been made in the last decade to validate these models against experimental results. A wide overview on the progress in understanding core transport in tokamaks is presented in [26], including examples of the validation of QL models against present experiments. Some recent TGLF validation carried out for DIII-D and AUG plasma discharges is reported in [27–30], while recent QLK validation works are presented in [24, 31–34] for hybrid, baseline, and mixed-isotope JET experiments. Bearing in mind that DTT will operate in a $T_{\mathrm{e}} > T_{\mathrm{i}}$ regime, a particularly relevant validation work is that presented in [35], with results on both TGLF and QLK modelling of an extensive set of experimental results from AUG and JET-ILW in regimes with high $T_{\mathrm{e}}/T_{\mathrm{i}}$.

In this paper, the the two most recent versions of TGLF have been used: TGLF SAT1-geo, released in November 2019, featuring an improved description of geometrical effects and calibration against CGYRO non-linear simulations, and TGLF SAT2, released in January 2021, featuring further improvements and better agreement with CGYRO as discussed in [36]. In runs with QLK, a recent release of the model [37] with improved trapped electron mode (TEM) treatment, thanks to a revised collision operator, has been employed. For QLK, in addition to this new official version, an ad hoc version of this model, where the TEM electron heat flux has been multiplied by a factor of 2 to match the gyrokinetic simulations described in section 3.5.4, has also been tested. This ad hoc retuning is physically justified by the fact that the region inside the mid-radius in DTT is strongly dominated by TEM, which is challenging for QLK. The ad hoc QLK correction is not intended to be a recommendation of a general prescription here, but rather a form of uncertainty quantification by modifying the model to account for known physics deficiencies for this specific case. In all QLK runs, the EM stabilisation mock-up [34] has been turned off because of the $T_{\mathrm{e}} \gg T_{\mathrm{i}}$ regime of DTT scenarios, which is outside the regime where the mock-up was developed.

For reasons of numerical stability, a small fraction (3%) of Bohm transport is added to the main turbulent transport. For electron heat transport, the neoclassical component of which is negligible, an additional diffusivity $\chi = 0.5\ \mathrm{m}^2\ \mathrm{s}^{-1}$ has been added in the region $\rho_{\mathrm{tor}} < 0.2$, where the turbulence level tends to vanish.

In order to set-up the runs in a faster way, simulations with the QLK neural network (QLKNN) [38] model have been also carried out, applying the QLKNN-hyper-10D version. This work has been also useful in testing the proper functioning of the QLKNN in DTT regime conditions.

The neoclassical transport is calculated by the Romanelli–Ottaviani model [39] for impurities and NCLASS [40] for main particles.

The toroidal rotation is predicted using a theory-driven empirical model [41, 42], in which the inward momentum pinch is included in the simulation thanks to the construction of a pinch number $RV_{\phi}/\chi_{\phi}$ that has the trend $RV_{\phi}/\chi_{\mathrm{i}} \propto -\sqrt{r/R}$ given by [41], is null at the plasma centre, and is $\sim 2.5$ at $\rho_{\mathrm{tor}} = 0.4$. The choice of those conditions is based on an analysis of some plasma parameters and the experimental pinch number dependence on those parameters found out in [42]. The Prandtl number $\chi_{\phi}/\chi_{\mathrm{i}}$ is fixed at 0.7; i.e. in place of a calculated momentum transport coefficient $\chi_{\phi}$, the produc t $0.7\chi_{\mathrm{i}}$ is used, where $\chi_{\mathrm{i}}$ is the ion thermal transport coefficient. The choice of 0.7 also empirically accounts for the component of the residual stress due to $E \times B$ shearing, which lowers the nominal Prandtl number. The rotation pedestal has been arbitrarily assumed to be 10 krad $\mathrm{s}^{-1}$ from present devices; in any case we note that the simulation is mainly influenced by the rotation gradient, not by its absolute value.

The heating and current drive (HCD) systems are modelled self-consistently in JINTRAC runs with suitable codes, as described in section 3.4. The particle source from NBI is also calculated, whilst the edge neutral penetration is negligible inside $\rho_{\mathrm{tor}} = 0.94$.

In our integrated modelling, argon (Ar, $A \simeq 40$, $Z = 18$) and tungsten (W, $A \simeq 184$, $Z = 74$) are included as impurities. Argon is a seeding gas used to enlarge the edge radiative dissipation decreasing the divertor power load, while tungsten comes from the divertor.

In JINTRAC runs, impurity densities and radiation are simulated up to the separatrix with SANCO [43]. For both gases, all ionisation states are treated separately by SANCO. In order to conserve the particle number equal to the initial value, the escape velocity, neutral influx and recycling factor are set as null. A radially constant effective charge equal to $Z_{\mathrm{eff}} = \sum_{\mathrm{i}} Z_{\mathrm{i}}^2 n_{\mathrm{i}}/n_{\mathrm{e}} = 1.7$ (sum over ion species) and a density ratio $n_{\mathrm{W}}/n_{\mathrm{Ar}} = 0.05$ are used as initial conditions.

Evaluating the neutron rate is a key point in the tokamak design because the neutron shields have to be able to withstand the neutron loads. In the JINTRAC simulations, the total neutron number is calculated as the sum of the neutrons produced by the fusion reactions between two thermal nuclei, between a thermal nucleus and a fast nucleus of the NBI beam, and

between a thermal nucleus and a fast nucleus of the ICRH minority species.

Sawteeth and ELMs are not included in the modelling, with the exception of the simulations described in section 3.5.3, where a continuous model for ELMs has been used. The absence of sawteeth implies that the profiles presented here correspond to the saturated recovery after a sawtooth crash.

### 3.2. JINTRAC & ASTRA

The DTT simulations have mainly been carried out with the JINTRAC suite with the JETTO [44] transport solver. The JINTRAC system includes several interfaced tokamak physics codes ($\sim 25$ modules) and has been used extensively for decades with experimental data of different tokamaks and to predict future devices. The 1.5D core plasma fluid code JETTO is the central part of JINTRAC, designed to calculate plasma profiles up to the separatrix. The JINTRAC suite has been used for full physics simulations of DTT using QLK or QLKNN, predicting current density and equilibrium, temperature, density (main ion and impurities), rotation, and heating, as described in section 3.1.

In addition, the ASTRA transport solver has also been used, within an iterative ASTRA–JINTRAC scheme devised for some high complexity cases with TGLF as turbulent transport model, due to the low speed of JINTRAC TGLF runs with DTT parameters. The starting point of this mixed method is running a JETTO simulation with QLK and using the resulting pro files as inputs for ASTRA. Then, an ASTRA run predicts temperature and density with fixed current density, heating, toroidal rotation, impurities, and radiative power, taken from JINTRAC. In this run, the equilibrium is solved self-consistently with the SPIDER [45] code. Impurities are included but not evolved in ASTRA; their profiles are set proportional to the electron density $n_e$ with a constant that reflects the JINTRAC settings. The impurity ionisation profiles are those provided by JINTRAC. As third step, the ASTRA profiles of density and temperatures are kept fixed in a new JETTO run aimed at recalculating the heating and safety factor profiles. The second and the third phases are repeated until convergence. This mixed ASTRA–JINTRAC approach is quite efficient because ASTRA TGLF simulations are much faster than JETTO TGLF runs and one iteration usually is enough.

### 3.3. Equilibrium

The expected standard operational points of DTT (with $R_0 = 2.14$ m) in terms of on-axis toroidal magnetic field $B_t$ and plasma current $I_{pl}$ are the following:

- full current and full field operational point, with $I_{pl} = 5.5$ MA and $B_t = 6$ T;
- reduced current and full field operational point, with $I_{pl} = 4.0$ MA and $B_t = 6$ T;
- reduced current and half field operational point, with $I_{pl} = 2.0$ MA and $B_t = 3$ T.

For these simulations, reference DTT plasma equilibria with average triangularity $\langle\delta\rangle \simeq 0.3$, major radius $R_0 = 2.14$ m, and minor radius $a = 0.65$ m for each of these standard operational points have been provided by the free boundary CREATE-NL [46] solver.

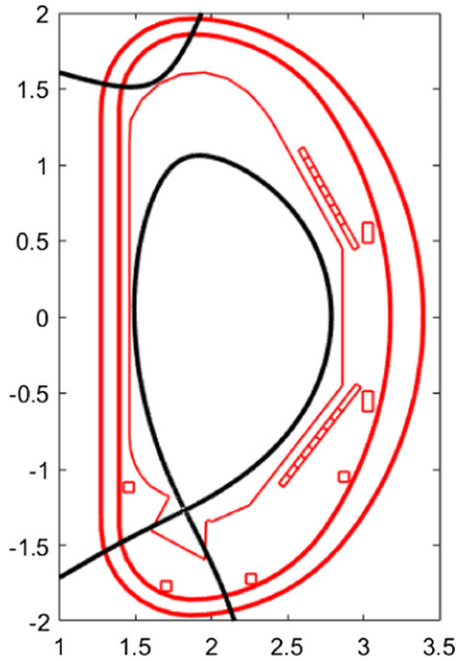


**Figure 2.** Plasma shape of the SN DTT scenario.

In the JETTO simulations, the MHD equilibrium is self-consistently recalculated 3 times per second by the equilibrium solver ESCO integrated in the suite. The plasma boundary is kept fixed to that of the CREATE-NL reference. The plasma shape of the SN DTT scenario at the full current and full field operational point is shown in figure 2.

At the flux surface that contains the 95% of the poloidal flux, performed simulations of DTT FP scenarios returned triangularity values in the range $\delta_{95} = 0.29$–$0.31$, elongation values in the range $k_{95} = 1.66$–$1.69$, and safety factor values in the range $q_{95} = 2.6$–$2.7$.

### 3.4. Heating and current drive (HCD)

Since DTT will be equipped with three auxiliary heating systems, the integrated simulations of this device feature high complexity level. The ECRH, ICRH, and NBI power depositions are computed several times during the runs, including the synergy effects.

In the heating configuration of FP option D, which has become the new reference option for the FP scenario, there are 4 ECRH clusters. Each cluster is composed of eight gyrotrons at 170 GHz, with an installed power of 1–1.2 MW from each gyrotron. Depending on the access port, these eight gyrotrons are divided into two upper (UP) gyrotrons, three equatorial top (EQT) gyrotrons, and three equatorial bottom (EQB) gyrotrons. A loss factor before launchers of 0.9 is evaluated, leading to the ECRH power at plasma of around 30.2 MW.

The ICRH system of DTT is designed to operate in the frequency range 60–90 MHz. In the reference $B_t = 6$ T scenario, the cyclotron resonances of $^3$He and H minorities are located on-axis when the ICRH frequency is 60 MHz and 90 MHz,

respectively. The system is devised in modular units, placed in equatorial ports, and each module is based on a pair of two-strap antennas. In order to better cope with abrupt coupling changes because of L–H transitions or ELMs, the two antennas of a module are fed in parallel. Since the power supplied by each RF antenna is 2 MW, supposing an efficiency of 0.75 (typical efficiencies for transmission lines and antenna coupling are 80% and 90%), the ICRH coupled power is ∼1.5 MW per antenna. The installation of the first RF module is scheduled for the initial phase. Depending on the FP option choice, an upgrade with one or two modules more may be realised. Importantly, the FP option D heating configuration includes two ICRH modules.

Due to the high DTT densities, to allow a central NBI power deposition during the flat-top plasma discharge phase, a negative ion-based NBI system at high energies $E > 300$ keV must be used in DTT. During early current ramp-up, late current ramp-down, and low current scenarios the employment of the NBI system must be cautiously evaluated, in order to avoid shine-through risks. Moreover, an important feature of the NBI system is its current drive capability and central fuelling. The FP option D heating configuration includes only one NBI, which provides ∼10.0 MW of power to the plasma, with a 500 keV deuterium beam. In the day-1 scenario, this injector will be used at reduced energy (∼400 keV) supplying a NBI power amount ⩽7.5 MW to the plasma.

The RF antenna, NBI injectors, and ECRH gyrotrons have been configured within the JINTRAC suite.

The ECRH power deposition is calculated every 0.25 s with the GRAY code [47]. Since DTT gyrotrons are too numerous to be included separately in GRAY (the maximum number is 20), they have been grouped into subsets. In the FP option D run, 12 beams are used (2 UP beams, 5 EQT beams, and 5 EQB beams). Each beam is simulated by the sum of one central ray and 160 rays arranged on 10 concentric rings and has a toroidal angle equal to 2°. In simulations of FP and day-1 scenarios all beams are injected in O-mode. Due to the lower magnetic field value, in the day-0 scenario the EC power is expected to be absorbed at the second harmonic. Since the O-mode polarisation is known to be less efficient at the second harmonic, the ECRH system will be used in X-mode for the day-0 case to maximise the absorption. The poloidal angles have been set in the following ranges: 43°–44° for UP beams, 2°–6° for EQT beams, and (−13°)–(−15°) for EQB beams.

The NBI power deposition is calculated using the PENCIL code [48]. Since the DTT NBI source is composed by negative ions, all beam particles are injected at the nominal energy. Hence, in PENCIL the full energy fraction has been set equal to 1. The total loss of NBI fast particles, considering both prompt and ripple losses, has been assessed at ∼4% in [49] and hence is considered negligible.

The PION [50–52] code calculates the ICRH power deposition, including the synergy effects with NBI. In the performed simulations hydrogen has always been used as the minority species with a concentration of 5% and the RF frequency has been set to 90 MHz. Thus, the cyclotron resonance is located where the magnetic field is equal to $B \simeq 5.9$ T, i.e. at $\rho_{\rm tor} \sim 0.15$.

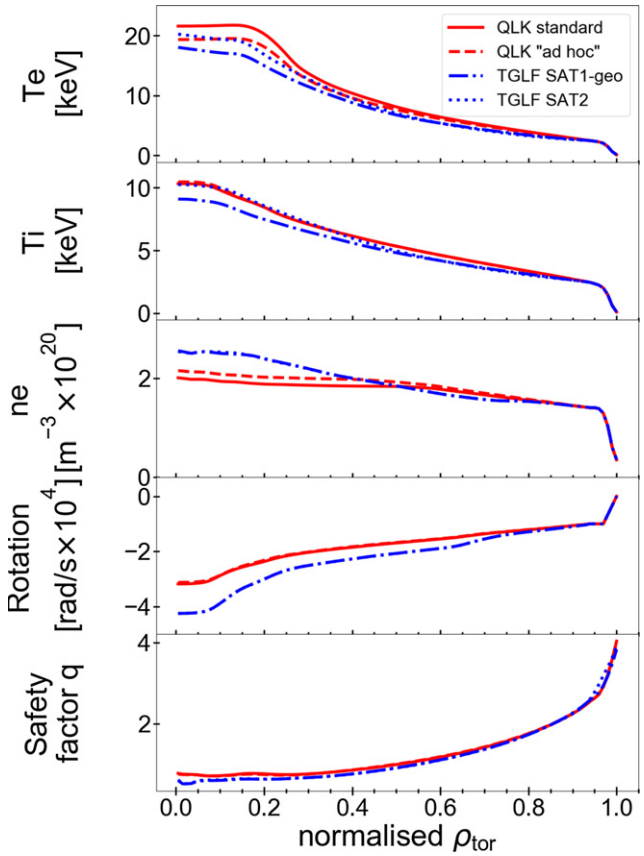


**Figure 3.** Steady-state radial profiles of the electron and ion temperatures, electron density, toroidal rotation, and safety factor of the FP option D scenario, with turbulent transport calculated by TGLF SAT1-geo (blue dash-dotted line) or SAT2 (blue dotted line) or by standard QLK (red solid line) or ad hoc QLK with TEM electron heat flux multiplied by a factor of 2 (red dashed line).

### *3.5. Full power option D scenario*

The commonly named option D has been selected as the new reference configuration for the FP scenario. In this configuration, auxiliary heating systems deliver a total power of ∼46 MW to the plasma: ∼10.0 MW from the NBI system, ∼6.0 MW from the ICRH system, and ∼30.2 MW from the ECRH system.

*3.5.1. Simulations with QLK or TGLF of full power option D scenario.* The integrated modelling of a steady-state deuterium plasma in the FP option D scenario has been performed using both the standard QLK model and an ad hoc QLK version in a JETTO run and the TGLF SAT1-geo or SAT2 model with the JINTRAC-ASTRA approach.

The electron temperature $T_{\rm e}$, ion temperature $T_{\rm i}$, electron density $n_{\rm e}$, toroidal rotation $\omega_{\rm tor}$, and safety factor $q$ radial profiles obtained by these four runs are shown in figure 3. The radial profiles of all power densities and those of the total electron and ion powers are displayed in figures 4(*a*) and (*b*), respectively, only for the standard QLK simulation. The power density and total power profiles resulting from the other three runs are similar in shape and size. The current density radial profile and its main contribution are shown in figure 5.

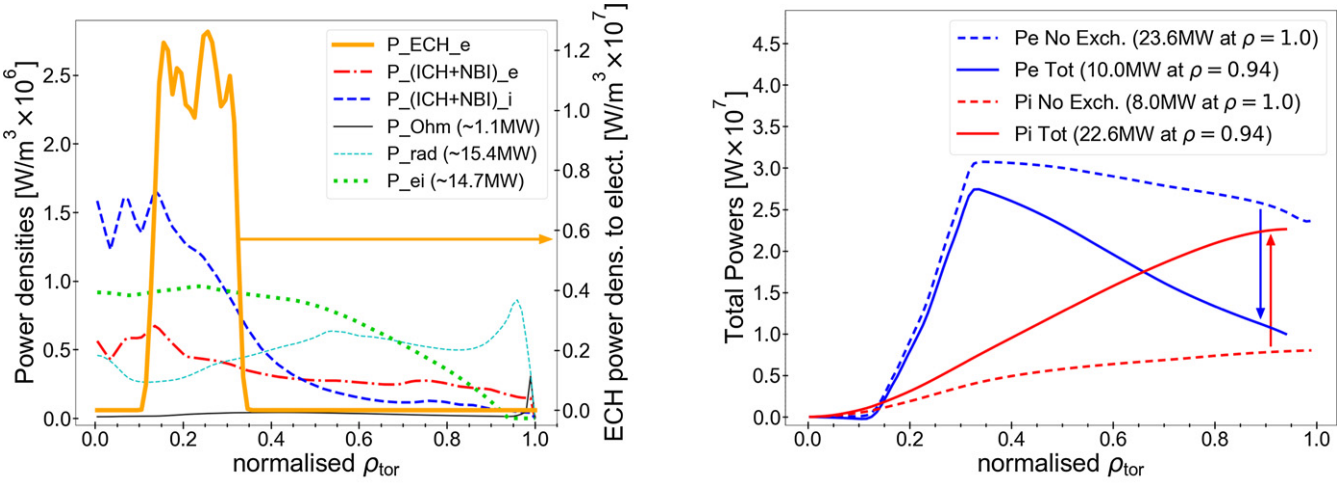


(a) Power densities. (b) Volume integrated powers.

**Figure 4.** (*a*) Radial profiles of power densities: ECRH power deposited to electrons $P_{\mathrm{ECHe}}$, NBI and ICRH power deposited to electrons $P_{(\mathrm{ICH+NBI})\mathrm{e}}$, NBI and ICRH power deposited to ions $P_{(\mathrm{ICH+NBI})\mathrm{i}}$, Ohmic power $P_{\mathrm{Ohm}}$, radiative power $P_{\mathrm{rad}}$, and thermal exchange power between electrons and ions $P_{\mathrm{ei}}$. (*b*) Radial profiles of electron and ion total powers including or excluding the thermal exchange power between species.

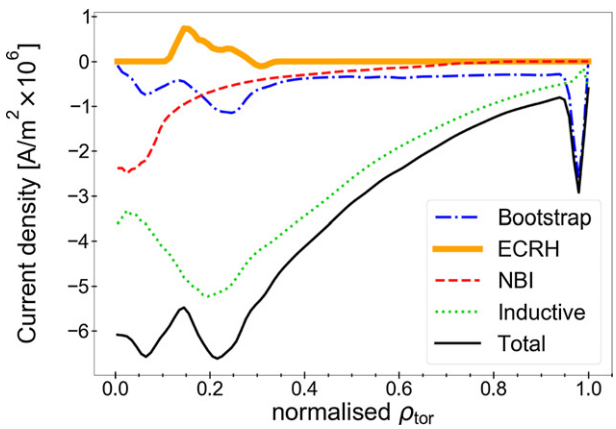


**Figure 5.** Radial profiles of the total current density and of its main contributions.

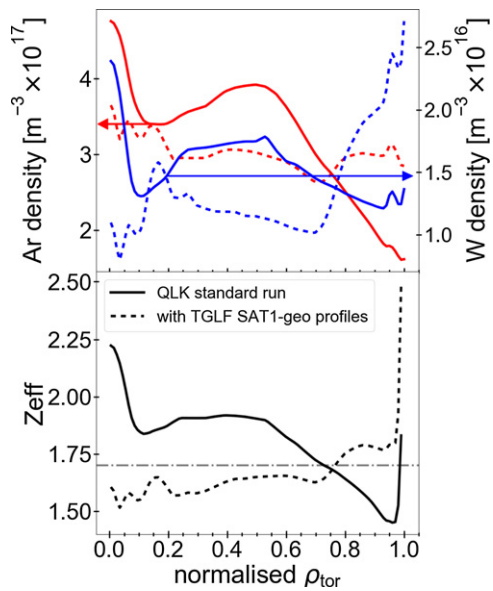


**Figure 6.** Radial profiles of the impurity densities (argon in red, tungsten in blue) and of the effective charge $Z_{\mathrm{eff}}$. The standard QLK case results (solid lines) are compared to an assessment of the impurity and $Z_{\mathrm{eff}}$ profiles in the presence of TGLF SAT1-geo predicted profiles carried out with JETTO/SANCO and QLK (dashed lines).

From figure 3, we note that the profiles of $T_{\mathrm{e}}$ and $T_{\mathrm{i}}$ reach maximum values in the range of 18.0–21.6 keV and in the range of 9.1–10.4 keV, respectively. There is a good agreement between TGLF and QLK temperature profiles, which are somewhat smaller in the TGLF SAT1-geo run, up to differences of the order of ∼15%–20% at the plasma centre, because of a slight difference in the temperature gradient in the region $0.65 \lesssim \rho_{\mathrm{tor}} \leqslant 0.94$. Electron densities of the two models present a good agreement for $\rho_{\mathrm{tor}} \gtrsim 0.5$, but a non-negligible discrepancy appears inside. Specifically, $n_{\mathrm{e}}$ has a moderately peaked profile in the TGLF simulation, while the QLK density profile is extremely flat in the inner half of the plasma. Due to a quite different $n_{\mathrm{e}}$ gradient in $0.2 \lesssim \rho_{\mathrm{tor}} \lesssim 0.5$, the maximum $n_{\mathrm{e}}$ value sweeps from $2.0 \times 10^{20}$ m$^3$ to $2.6 \times 10^{20}$ m$^3$. In order to identify the most reliable prediction and to explain the difference of density peaking between TGLF and QLK, a benchmark work of the two QL models against the gyrokinetic model GENE [53, 54] in the DTT parameter range has been performed and its results are displayed in section 3.5.4.

Comparing the modelling results between the standard QLK version and the QLK version with $2 \times q_{\mathrm{e,TEM}}$, we noted that the 'ad hoc' model introduced small variations in the right direction. Specifically, the density peaking is somewhat increased (closer to the TGLF one) in the 'ad hoc' QLK density profiles. Nevertheless, these improvements are too small

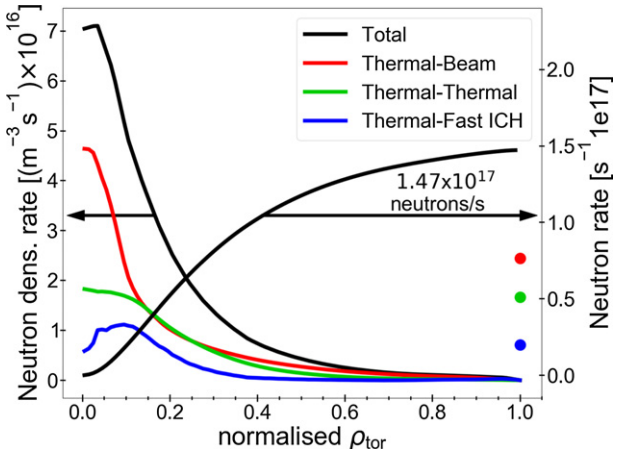


**Figure 7.** Radial profiles of neutron density rates, where neutrons are produced by fusion reactions between two thermal nuclei (green), between a thermal nucleus and a fast nucleus of the NBI beam (red), between a thermal nucleus and a fast nucleus of the ICRH minority species (blue), and between any pair of nuclei (black). The radial profile of the total neutron rate is also displayed (black), with points indicating the three contributions to it. These profiles are for the TGLF SAT2 FP case.

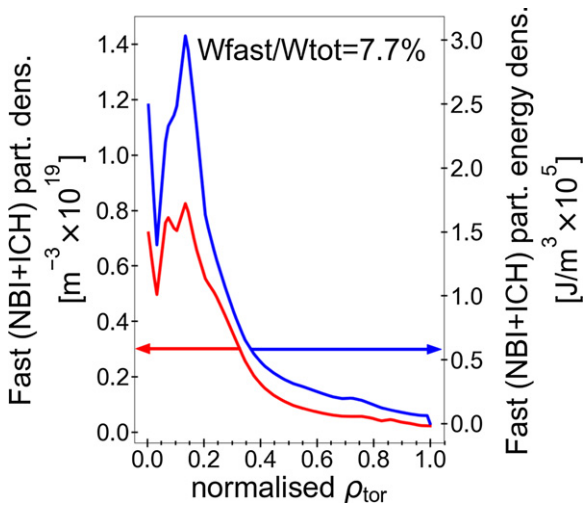


**Figure 8.** Radial profiles of density and energy density of energetic particles due to the NBI and ICRH systems.

to justify the employment of this QLK version in further simulations.

With both QLK and TGLF models, it turns out that DTT is characterised by $T_e$ significantly larger than $T_i$, particularly in the inner half of the plasma. This is due to the very large and localised ECH power density ($P_{ECHe} \sim 1.1 \times 10^7$ W m$^{-3}$) and to the fact that $T_e/T_i$ is a key factor determining the ion critical gradient $\left(R/L_T\right)_{crit}$ [55, 56], lowering it with increasing $T_e/T_i$. The low ion temperature gradient (ITG) threshold in the presence of a high ion stiffness then prevents $T_i$ from peaking. This behaviour is in line with several observations in present-day tokamaks and stellarators with high electron heating; see for example the recent work in [57]. Instead $T_e$ is largely determined by TEMs, which exhibit much lower stiffness and typically higher $\left(R/L_{T_e}\right)$ thresholds so that a higher $T_e$ peaking

**Table 2.** FP option D scenario dimensionless quantities.

| | TGLF SAT1-geo | TGLF SAT2 | QLK Standard | QLK Ad hoc |
|---|---|---|---|---|
| $\tau_E$ $(P = P_{tot})$ | 0.25 | 0.27 | 0.27 | 0.28 |
| $\tau_E$ $(P = P_{sep})$ | 0.43 | 0.42 | 0.41 | 0.43 |
| $H_{98}$ $(P = P_{sep})$ | 0.95 | 1.00 | 0.99 | 0.98 |
| $\beta_{N_{therm}}$ (%) | 1.39 | 1.47 | 1.49 | 1.51 |
| $\beta_{N_{tot}}$ (%) | 1.49 | 1.57 | 1.62 | 1.62 |
| $W_{EP}/W_{tot}$ (%) | 6.5 | 6.7 | 7.7 | 6.7 |
| $\langle n_e \rangle / n_G$ | 0.44 | 0.44 | 0.40 | 0.42 |

can be reached. The ITG modes and TEMs are dominant in these plasmas, while ETG modes [58], which are included in the integrated simulations, do not play an important role, due to the high $T_e/T_i$. The ETG unimportance was evident from both stand-alone runs and profile simulations performed with TGLF and with QLK with and without ETG inclusion. Moreover, the linear gyrokinetic runs carried out with GENE also confirmed the lack of ETG contribution.

Locally, in the DTT FP scenario, electron heating dominates in the inner plasma region, as evidenced by figure 4(*b*). Since the ion channel is very stiff and bound to a low critical gradient due to $T_e/T_i > 1$, ions represent a big power sink through collisional exchange. The ion temperature profile results stuck near the threshold irrespective of the large amount of supplied power.

Globally, the core radiated power $P_{rad} \approx$ 15.4–17.8 MW is about the 35% of the total power, the ohmic power $P_{Ohm} \approx$ 1.1 MW is quite negligible, and a large amount of power (13.7 MW $\lesssim P_{ei} \lesssim$ 14.7 MW) is exchanged from electrons to ions because of the collisional coupling. Therefore, although the external electron power $P_{e\ ext} \approx$ 38 MW is much bigger than the external ion power $P_{i\ ext} \approx$ 8 MW, globally the total electron power $P_{etot} \approx$ 9.5–10.4 MW is much lower than the total ion power $P_{itot} \approx$ 21.8–22.6 MW. In DTT, the collisional time is higher than the confinement time, so the collisional exchange is not enough to equilibrate $T_e$ and $T_i$. As things stand, obtaining an ion temperature profile as high as possible would be beneficial; to achieve this, one would have to find ways of reducing the ion stiffness or increasing the ITG threshold, in addition to having more central ion power. The choice of the option D as the FP reference scenario has been based on this principle. In particular, some EM stabilisation effects are known to reduce ion stiffness and they can be increased by the presence of fast ions [59, 60]. These considerations have led to the choice of increasing the ICRH power to the maximum technically feasible and increasing the NBI energy with respect to the original proposal described in [6].

From figure 3, we also note that the safety factor value at the flux surface that contains 95% of the poloidal flux is quite low, $q_{95} \approx$ 2.5–2.6. An increased disruptivity is observed in plasma with such low $q_{95}$; see e.g. [61]. As a consequence, the DTT team decided to enlarge the DTT major radius from $R_0 = 2.14$ m to $R_0 = 2.19$ m and its minor radius from $a = 0.65$ m to $a = 0.70$ m to bring $q_{95}$ nearer to 3.

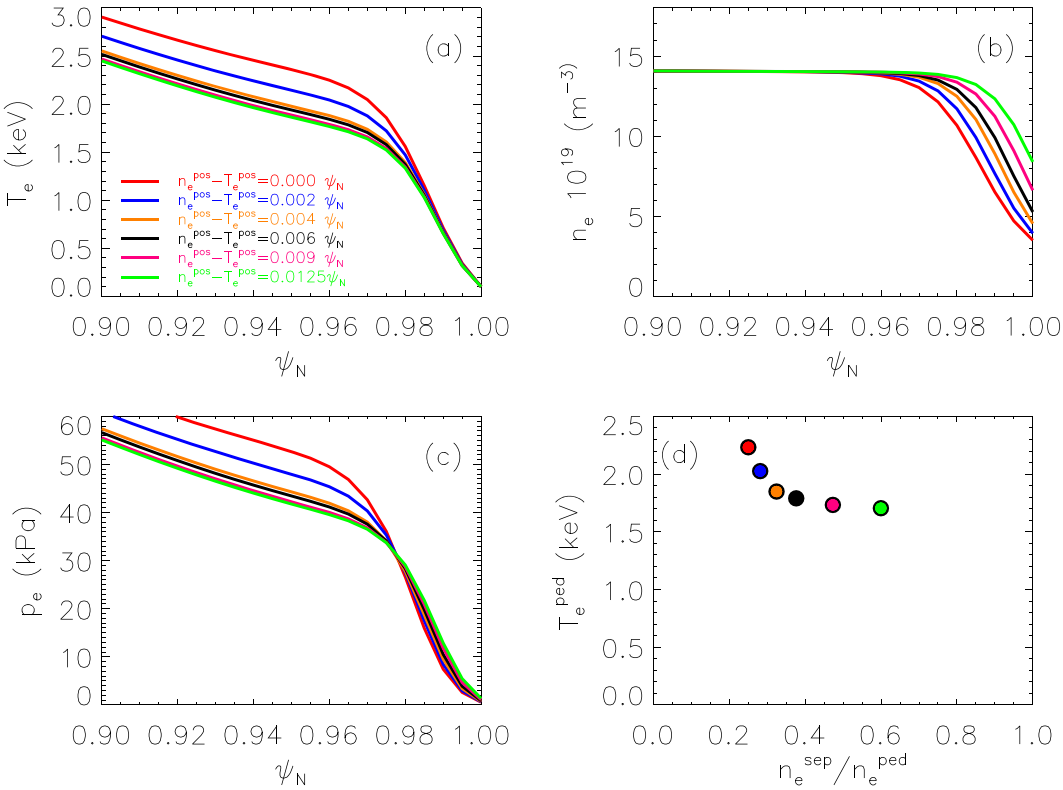


**Figure 9.** Profiles of (*a*) electron temperature, (*b*) density, and (*c*) pressure in the pedestal region for different values of relative shift ($n^{\rm pos} - T^{\rm pos}$) ($\psi_N$). (*d*) Electron temperature at the pedestal top $T_{\rm e}^{\rm ped}$ as a function of $n_{\rm e}^{\rm sep}/n_{\rm e}^{\rm ped}$.

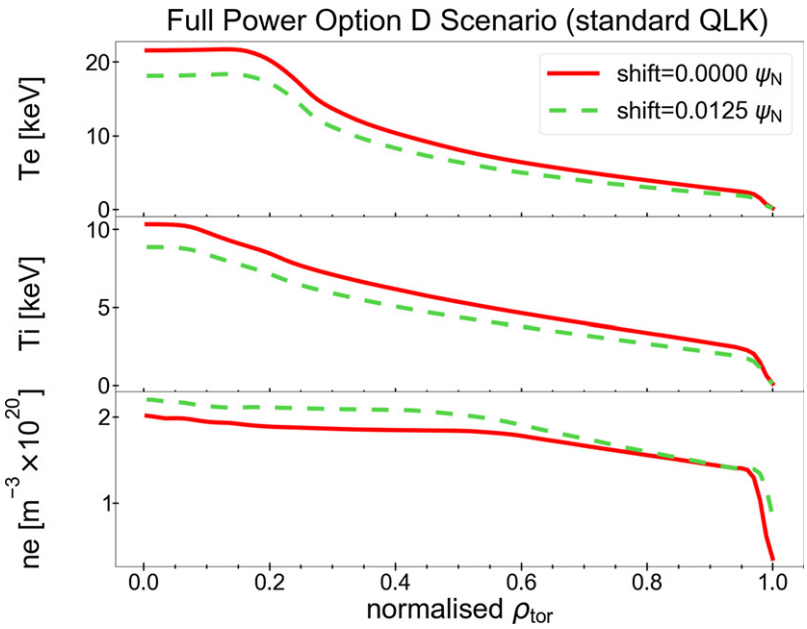


**Figure 10.** Radial profiles of electron temperature, ion temperature, and electron density predicted by JETTO runs using the standard QLK model for different values of relative shift (the red lines correspond to a null shift, while the green lines correspond to a shift of 0.0125$\psi_N$).

Within the JINTRAC runs, the contribution of impurities is calculated by SANCO, using neoclassical transport and turbulent transport from QLK. In figure 6, the density profiles of impurities and the profile of the effective charge $Z_{\rm eff}$ are displayed for the QLK case with solid lines. The TGLF simulations in ASTRA do not evolve impurity species, but only take into account their effects assuming the $n_{\rm e}$ profile shape. Nevertheless, it is interesting to get an idea of which argon and tungsten densities would be computed by QLK for $T_{\rm e}$, $T_{\rm i}$, and $n_{\rm e}$ values such as those in the TGLF case. Thus, a JETTO run with interpretative $T_{\rm e}$, $T_{\rm i}$, and $n_D$ profiles equal to the TGLF SAT1-geo case has been performed, including SANCO calculations

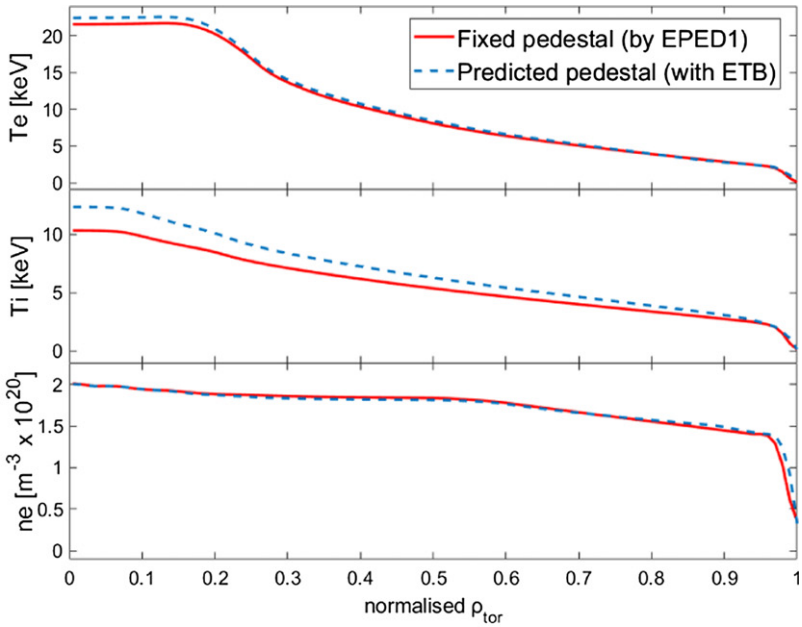


(a) Whole radial profiles.

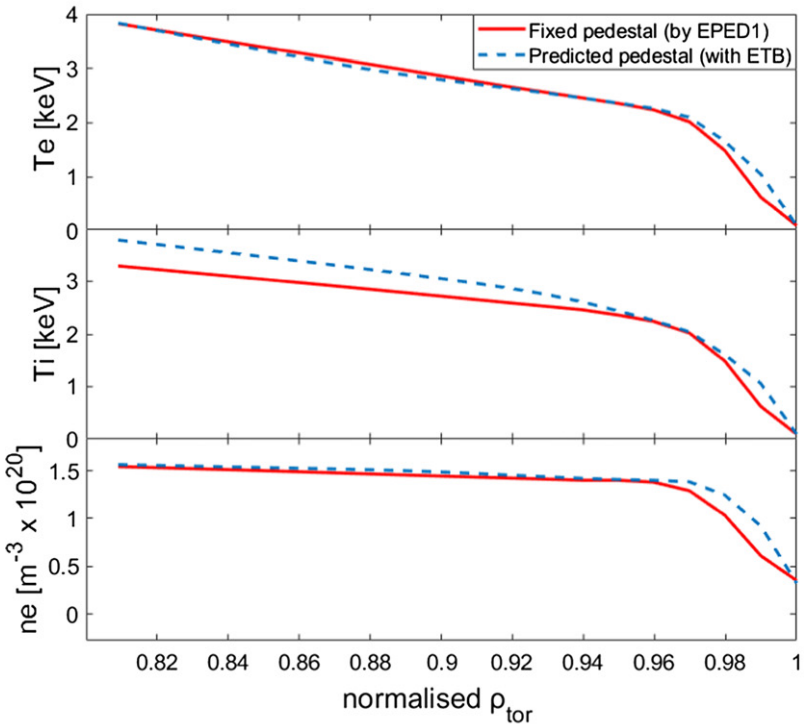


(b) Profile zoom in the pedestal region.

**Figure 11.** Comparison of $T_e$, $T_i$, and $n_e$ radial profiles between the standard QLK case with the fixed pedestal of section 3.5.1 (solid red lines) and the new standard QLK case with the moulded ETB (dashed blue lines).

for impurity densities and using QLK as a turbulent transport model for the impurities. This allows us to estimate the effect of the TGLF electron density peaking on the impurity profiles, as shown in figure 6 with dashed lines.

Argon and tungsten densities amount to $n_{Ar}/n_e \approx 0.28\%$ and $n_W/n_e \approx 0.014\%$, respectively. We observe some penetration of the impurities into the core in both models.

In future works, other possible seeding gasses will be tested in place of argon to investigate their effect on the edge radiative dissipation.

The largest neutron loads to be coped with obviously occur in the FP scenario. The more challenging prospect in this respect is represented by the TGLF SAT2 FP run, where the maximum value of neutron rate is reached. The

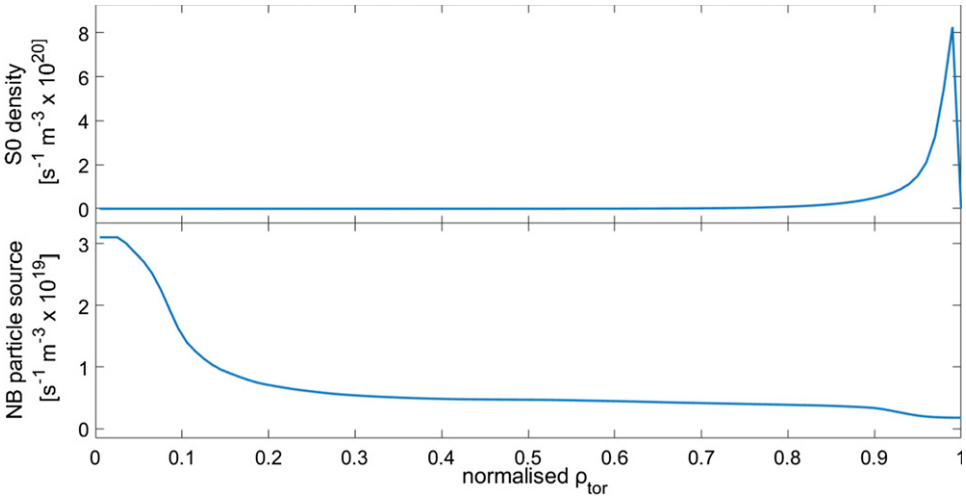


**Figure 12.** Radial profile of the source of neutrals from the edge and radial profile of the NBI particle source.

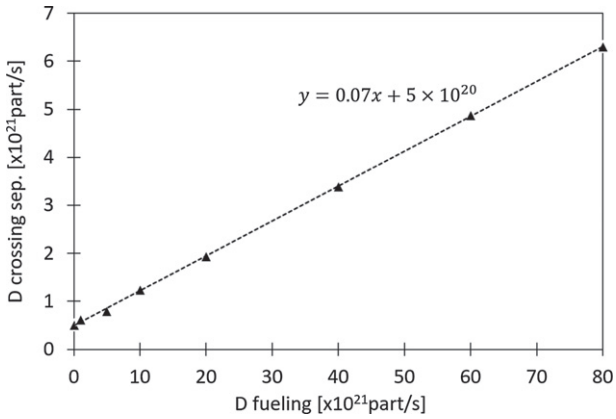


**Figure 13.** Dependence of neutral penetration across the separatrix on deuterium fuelling as derived from SOLEDGE2D-EIRENE simulations.

total neutron density rate and the radial profiles of its three contributions shown in figure 7 are for the run outcome with the TGLF SAT2 profiles. When integrating over the entire profile up to the separatrix, the total neutron rate amounts to $1.47 \times 10^{17}$ neutrons $s^{-1}$, compatible with the present design of neutron shields with a good safety margin. The neutron density rates obtained from simulations with standard or ad hoc QLK or with TGLF SAT1-geo profiles are somewhat lower, but definitely similar in shape, giving total neutron rates in the range of $1.29$–$1.36 \times 10^{17}$ neutrons $s^{-1}$. In all cases, the largest contribution is given by the fusion reactions between NBI fast deuterium and thermal deuterium, but the thermal–thermal neutrons are also very significant.

In figure 8 the density and energy density radial profiles of energetic particles are shown for the standard QLK run. The EP profiles in the TGLF SAT2, TGLF SAT1-geo, and ad hoc QLK cases present similar shapes. In the FP reference scenario, the energy fraction owned by the EPs amounts to $W_{\mathrm{EP}}/W_{\mathrm{tot}} \approx$ 6.5%–7.7%.

For the sake of completeness, table 2 presents the main dimensionless physical quantities of this scenario. Of particular note, the total radiation from the plasma inside the separatrix can be subtracted or not from the input power when calculating the confinement, yielding the two $\tau_E$ values in table.

*3.5.2. Pedestal variations.* Core–edge integration is a key point in the DTT-integrated modelling work. Since the pedestal points are used as boundary conditions in the JETTO/ASTRA simulations, for the FP scenario we investigated the pedestal height variability depending on the Europed run inputs to examine the robustness of the central results of our analysis. Some Europed inputs (such as $I_{\mathrm{pl}}$, $B_{\mathrm{t}}$, $R_0$ etc) are imposed by the selected scenario and by general DTT parameters; therefore we have not performed sensitivity tests on these. We have tested the sensitivity to $\beta$ values in the range $0.4 \lesssim \beta_{\mathrm{pol}} \lesssim 0.8$ and verified that the effect is small. Then, the $\beta_{\mathrm{pol}}$ value has been selected iteratively to match the JINTRAC predicted value.

It has also been checked that $T^{\mathrm{sep}}$ value variations in the range of 100–200 eV did not lead to significant changes in the pedestal values. Neither substituting argon with an other impurity (for instance with neon as seeding gas) nor varying the $Z_{\mathrm{eff}}$ value around the reference value effectively impacts the pedestal height. All of these small $T_{\mathrm{e}}^{\mathrm{ped}}$ variations fall back into a typical accuracy of around $\pm 20\%$ of the EPED model when the pedestal is PB limited [17].

Although modelling the direct effect of the gas on the pedestal is outside the scope of this work, the effect of the gas is expected to increase $n_{\mathrm{e}}^{\mathrm{sep}}$ and shift the density position $n_{\mathrm{e}}^{\mathrm{pos}}$ outwards, as observed in AUG, JET-ILW, TCV, and DIII-D [18, 62–65]. Therefore, we have assessed the gas effect on the pedestal by testing the impact of the density position on the predicted $T_{\mathrm{e}}^{\mathrm{ped}}$.

A null relative shift $\left(n_{\mathrm{e}}^{\mathrm{pos}} = T_{\mathrm{e}}^{\mathrm{pos}}\right)$ is the standard assumption in the basic EPED model and has been used throughout the paper. Assuming that the density has the same position as the temperature (corresponding to $n_{\mathrm{e}}^{\mathrm{sep}}/n_{\mathrm{e}}^{\mathrm{ped}} \approx 0.25$, i.e. to $n_{\mathrm{e}}^{\mathrm{sep}} \approx 3.5 \times 10^{19}$ $\mathrm{m}^{-3}$), the Europed run predicts $T_{\mathrm{e}}^{\mathrm{ped}} \approx 2.2$ keV.

**Table 3.** Reference parameters from the end of the ASTRA-TGLF simulation, at the radius of analysis $\rho_{\rm tor} = 0.32$, used as GENE inputs.

| $R/L_n$ | $R/L_{Te}$ | $R/L_{Ti}$ | $T_i/T_e$ | $n_{Ar}/n_e$ | $n_W/n_e$ |
|---|---|---|---|---|---|
| 2.99 | 7.8 | 3.93 | 0.59 | $1.5 \times 10^{-3}$ | $7.5 \times 10^{-5}$ |
| $q$ | $\hat{s}$ | $\kappa$ | $\delta$ | $\nu_c$ | $\beta_e$ |
| 0.76 | 0.31 | 1.38 | $4.9 \times 10^{-2}$ | $5.23 \times 10^{-5}$ | $2.75 \times 10^{-2}$ |

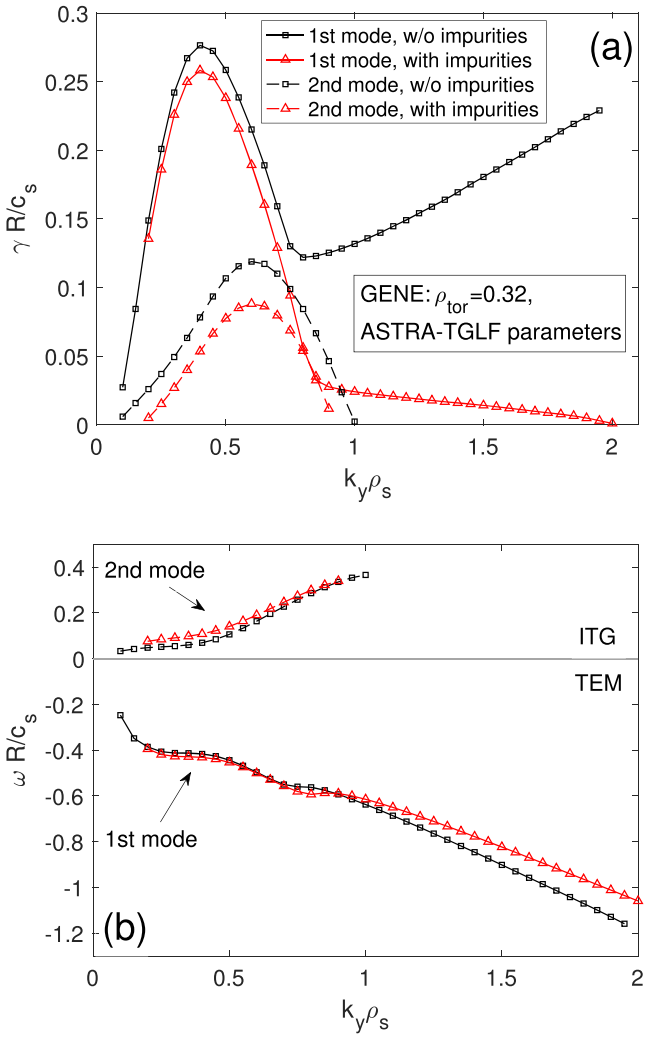


**Figure 14.** $k_y$ spectra of the growth rate $\gamma$ ($a$) and angular frequency $\omega$ ($b$) of the most unstable linear mode (solid) and of the second unstable linear mode (dashed), neglecting (black) or taking into account (red) the impurities, for ASTRA-TGLF parameters at $\rho_{\rm tor} = 0.32$. Both $\gamma$ and $\omega$ are normalised with $c_s/R$, while $k_y$ is normalised with $1/\rho_s$.

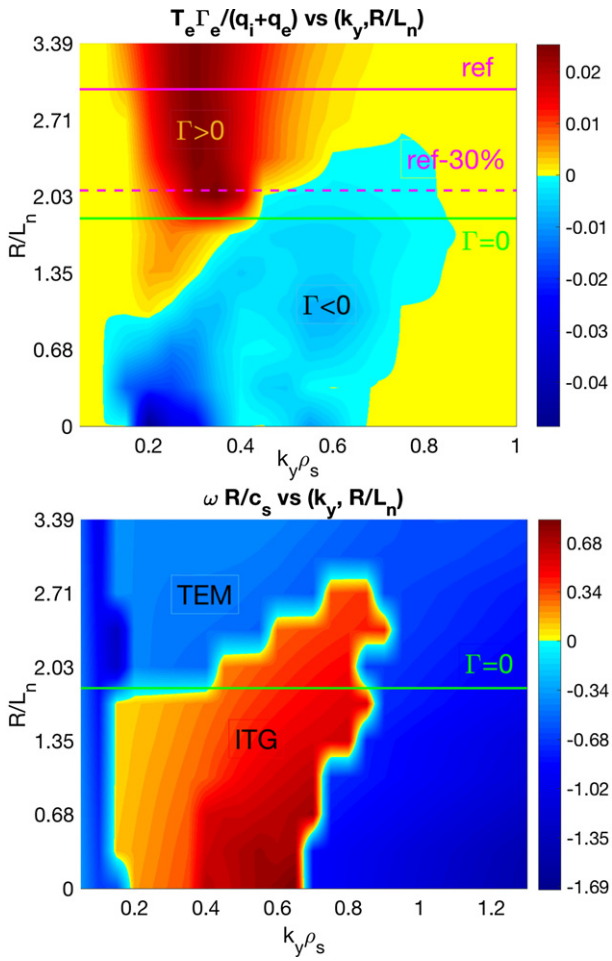


**Figure 15.** ($a$) Spectrum of the QL electron particle flux $\Gamma_e(k_y)$ versus $R/L_n$, normalised with $(q_e + q_i)/T_e$, where $q_e$ and $q_i$ are the total QL electron an ion heat fluxes and $\Gamma_e(k_y)$ satisfies $\Gamma_e = \sum_{k_y} \Gamma_e(k_y)$. ($b$) $k_y$ spectrum of the growth rate $\gamma$ of the most unstable linear mode versus $R/L_n$. $\gamma$ is normalised with $c_s/R$, while $k_y$ is normalised with $1/\rho_s$.

However, relatively recent results show that typically $n_e^{\rm pos} > T_e^{\rm pos}$, with values of the shift higher than $\approx 0.002\psi_N$ [18, 62]. The possible effect of $n_e^{\rm pos} > T_e^{\rm pos}$ has been tested, as displayed in figure 9.

By increasing the relative shift, $T_e^{\rm ped}$ decreases until saturation is reached above the relative shift $\approx 0.01\psi_N$ (corresponding to $n_e^{\rm sep}/n_e^{\rm ped} \approx 0.5$, i.e. to $n_e^{\rm sep} \approx 7 \times 10^{19}$ m$^{-3}$). The saturation is related to the effect of the density position on the pressure position, as discussed in [19]. In DTT, $n_e^{\rm sep}/n_e^{\rm ped} \lesssim 0.5$ is expected, and in the main simulations of this work $n_e^{\rm sep}/n_e^{\rm ped} \approx 0.2$–$0.3$. With this value, the EPED model is rather accurate (within 20%). The most recent results obtained in JET show that the shortfall compared to EPED occurs at relatively high separatrix density (approximately $n_e^{\rm sep}/n_e^{\rm ped} > 0.5$, with significant discrepancies that occur above 0.6) [66]. Nonetheless, to test the effect of possibly higher $n_e^{\rm sep}/n_e^{\rm ped}$, an Europed simulation has also been done at $n_e^{\rm sep}/n_e^{\rm ped} \approx 0.5$–$0.6$. This value is expected to already be relatively high for DTT,

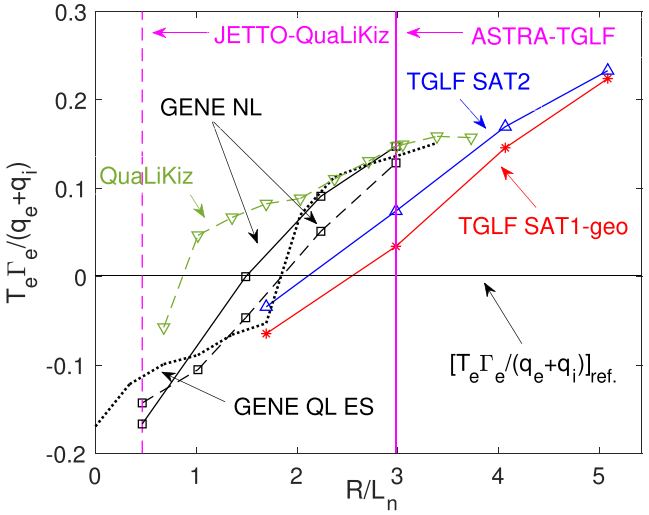


**Figure 16.** Normalised electron particle flux $T_e\Gamma_e/(q_e+q_i)$ vs $R/L_n$, with parameters from ASTRA-TGLF (solid or dotted) and JINTRAC-QLK (dashed) predictive transport simulations, computed with GENE NL (black), GENE QL (black, dotted), TGLF SAT1-geo (red), TGLF SAT2 (blue) and QLK (green), where the QL codes have been run using the stand-alone version. The reference values $R/L_n \sim 3$ (ASTRA-TGLF) and $R/L_n = 0.46$ (JINTRAC-QLK) are shown by solid and dashed vertical magenta lines, respectively.

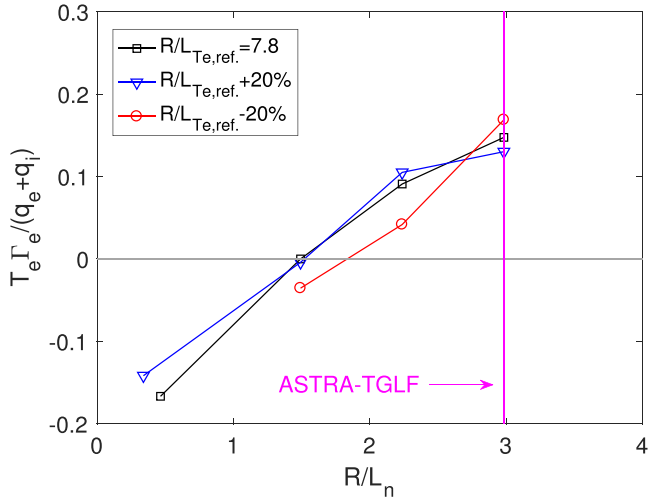


**Figure 17.** Normalised electron particle flux $T_e\Gamma_e/(q_e+q_i)$ vs $R/L_n$, for the three values $R/L_{Te} = 7.8, 7.8 \pm 20\%$ of the normalised electron temperature logarithmic gradient.

although not high enough to lead to major problems with the reliability of the EPED predictions [66]. Above $n_e^{sep}/n_e^{ped} \approx$ 0.5–0.6, there is presently no model to reliably assess the effect of the gas rate on the pedestal.

The minimum temperature reached with the highest relative shift of $0.0125\psi_N$ (with $n_e^{sep} \approx 8 \times 10^{19}$ m$^{-3}$, i.e. with $n_e^{sep}/n_e^{ped} \approx 0.6$) is $T_e^{ped} \approx 1.7$ keV, approximately 500 eV lower than the reference case.

In order to test the effects of the pedestal variations due to different relative shift values on plasma profiles, we repeated the standard QLK run of the FP reference scenario (with null relative shift) but we set the pedestal points calculated by EPED with a relative shift of $0.0125\psi_N$. Temperature and density radial profiles of these two simulations are compared in figure 10. We observe that the temperature value reduction at the top of the pedestal propagates inwards up to the plasma centre, but it is more interesting to note the increased density peaking as a consequence of a non-null pedestal relative shift.

Overall, however, the scenario predictions are not significantly affected.

*3.5.3. Fuelling issues.* In order to evaluate if the predicted density profiles can be sustained by only gas puffing or if a pellet fuelling system is required, the level of edge neutrals required to operate in the FP option D scenario without pellets has been investigated.

The standard QLK run of section 3.5.1 has been extended up to the separatrix by replacing the fixed pedestal externally calculated by Europed with the results of a suitable edge transport barrier (ETB) tuned to reproduce the Europed pedestal.

To calculate the neutral source, the FRANTIC [67] code has been included in the simulation, setting a feedback control of gas puffing to reach the electron density value expected at the top of barrier (TOB) with null recycling. The ETB transport coefficients are arranged to obtain the temperature at the top of the pedestal as close as possible to the Europed values, thanks to a continuous ELM model. In figure 11, the $T_e$, $T_i$, and $n_e$ radial profiles resulting from this adjustment work are compared to the profiles of the QLK case with a fixed pedestal to show the good agreement between them.

The neutral penetration into the plasma evaluated by FRANTIC is adequate for fuelling since the neutral density rate is up to $\rho_{tor} \sim 0.8$, as displayed in figure 12. The NBI contribution to the neutral source is small.

To reach the density value at the TOB which allows us to have $\langle n_e \rangle \sim 0.4\, n_G$ in the FP reference scenario, a neutral flux level of about $0.36 \times 10^{22}$ particles s$^{-1}$ at the separatrix is required.

The dependence of neutral penetration across the separatrix as a function of deuterium fuelling was found starting from the results obtained in [68] with the edge code SOLEDGE2D-EIRENE [69, 70]. A scan of the fuelling was performed starting from a detached case. The results are shown in figure 13; of particular note, $\sim 5 \times 10^{22}$ particles s$^{-1}$ is the deuterium fuelling corresponding to the required neutral flux at the separatrix. This means that we need a gas puffing and pumping system capable of supplying and pumping at least $\sim 5 \times 10^{22}$ particles s$^{-1}$, which is near the feasibility limit.

Due to this marginality, and in order to avoid degrading the edge plasma with extremely high gas puff rates, a pellet injection system is found to be useful as a fuelling method in DTT to minimise the operational risk.

A modelling work on pellets has just started. In addition, a work on core–pedestal–SOL-integrated modelling,

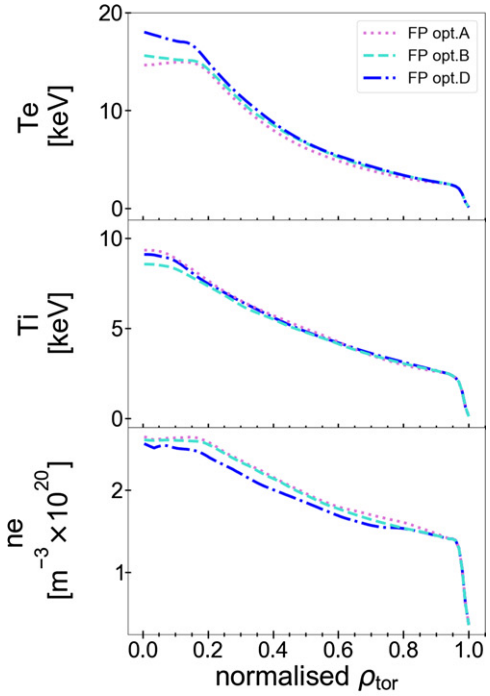


(a)

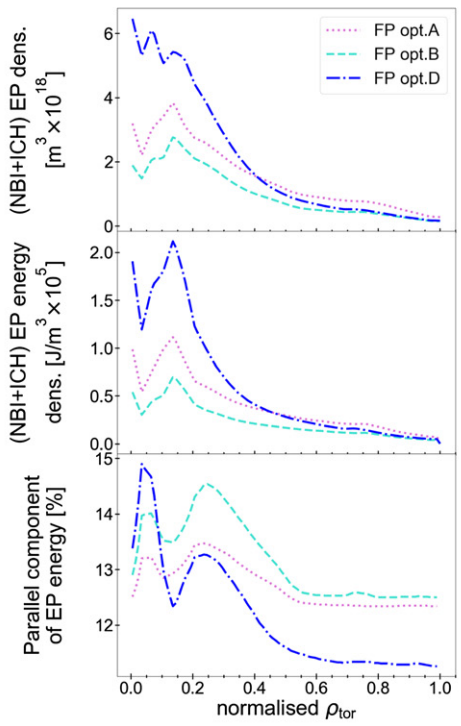


(b)

**Figure 18.** Comparison of radial profiles among the most salient options of the FP scenario. (*a*) Profiles of electron temperature, ion temperature, and electron density. (*b*) Profiles of energetic particle density, energetic particle energy density, and the parallel component of the energetic particle energies.

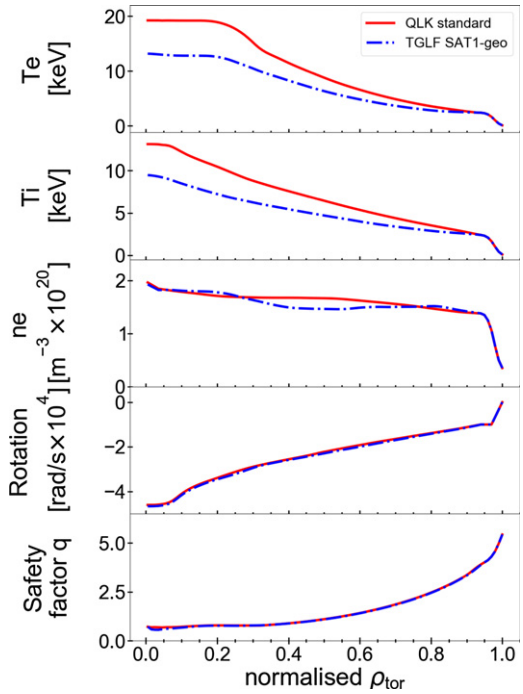


**Figure 19.** Steady-state radial profiles of the electron and ion temperatures, electron density, toroidal rotation, and safety factor of the day-1 scenario, with turbulent transport calculated by TGLF SAT1-geo (blue dash-dotted line).

totally self-consistent in terms of temperature and density profiles, fluxes, and transport coefficients, is envisaged as future development.

*3.5.4. Gyrokinetic simulations to validate QLK and TGLF for DTT full power parameters.* Linear and nonlinear (NL) gyrokinetic simulations have been performed at the fixed radius $\rho_{tor} = 0.32$, using the flux-tube (radially local) version of the GENE code, in order to characterise the turbulence, compute the particle and heat fluxes and estimate the density peaking, testing the results of the ASTRA-TGLF and JINTRAC-QLK predictive runs. This analysis has been carried out with the main goal of understanding which of the two transport simulations gives the more reliable estimate of the density peaking, since they give different results. The parameters from the end of the ASTRA-TGLF run have been used as GENE inputs. A detailed analysis of this case has been performed, and some parameters have been also replaced with the corresponding ones from the end of the JINTRAC-QLK simulation to investigate their impact on the results. The main simulation parameters (from ASTRA-TGLF) are summarised in table 3.

Argon and tungsten impurities with effective charge $Z_{eff} = 1.65$ have been accounted for as kinetic species in the simulations when not differently stated. The normalised radial logarithmic gradients of the $f$ profiles ($f = n, T$) are here defined as $R/L_f = -R\,\mathrm{d}\ln f/\mathrm{d}r$, where $R$ and $r$ are the plasma major and minor radii at the selected mag-

**Table 4.** Heating mix options (power values at plasma) evaluated for DTT FP scenarios.

| Option | ECRH | ICRH | NBI |
|---|---|---|---|
| A | ∼28.8 MW | ∼3 MW | ∼15 MW |
| | (32 gyr. × 1 MW) ×0.9 | (2 antennas in one module) | 2 inj. × (7.5 MW at 400 keV) |
| B | ∼36.0 MW | ∼3 MW | ∼7.5 MW |
| | (16 gyr. × 1 MW + 20 gyr. × 1.2 MW) ×0.9 | (2 antennas in one module) | 1 inj. × (7.5 MW at 400 keV) |
| C | ∼28.8 MW | ∼9 MW | ∼7.5 MW |
| | (32 gyr. × 1 MW) ×0.9 | (6 antennas in three modules) | 1 inj. × (7.5 MW at 400 keV) |
| D | ∼30.2 MW | ∼6 MW | ∼10 MW |
| | (24 gyr. × 1 MW + 8 gyr. × 1.2 MW) ×0.9 | (4 antennas in two modules) | 1 inj. × (10 MW at 500 keV) |
| E | ∼28.8 MW | ∼3 MW | ∼15 MW |
| | (32 gyr. × 1 MW) ×0.9 | (2 antennas in one module) | 1 inj. × (10 MW at 500 keV) + 1 inj. × (5.0 MW at 200 keV) |
| F | ∼28.8 MW | ∼3 MW | ∼10 MW |
| | (32 gyr. × 1 MW) ×0.9 | (2 antennas in one module) | 1 inj. × (10 MW at 600 keV) |
| G | ∼30.2 MW | ∼6 MW | ∼7.5 MW |
| | (24 gyr. × 1 MW + 8 gyr. × 1.2 MW) ×0.9 | (4 antennas in two modules) | 1 inj. × (7.5 MW at 400 keV) |
| H | ∼30.2 MW | ∼6 MW | ∼10 MW |
| | (24 gyr. × 1 MW + 8 gyr. × 1.2 MW) ×0.9 | (4 antennas in two modules) | 1 inj. × (10 MW at 400 keV) |
| I | ∼26.3 MW | ∼9 MW | ∼10 MW |
| | (16 gyr. × 1 MW + 11 gyr. × 1.2 MW) ×0.9 | (6 antennas in three modules) | 1 inj. × (10 MW at 500 keV) |

**Table 5.** Main parameters of a subset of heating options for the DTT FP scenario using TGLF SAT1-geo.

| Heating option | $\tau_E$ (s) ($P = P_{\rm tot}$) | $\tau_E$ (s) ($P = P_{\rm sep}$) | H98Y | $\beta_{\rm N_{therm}}/\beta_{\rm N_{tot}}$ | $W_{\rm EP}/W_{\rm tot}$ (%) | $T_{\rm e_0}/T_{\rm i_0}$ (keV keV$^{-1}$) | $\langle n_{\rm e}\rangle/n_{\rm G}$ | Neutron Rate |
|---|---|---|---|---|---|---|---|---|
| A | 0.25 | 0.45 | 0.95 | 1.40/1.49 | 5.7 | 14.6/9.3 | 0.47 | $1.24 \times 10^{17}$ s$^{-1}$ |
| B | 0.26 | 0.44 | 0.95 | 1.42/1.46 | 3.3 | 15.6/8.5 | 0.46 | $0.85 \times 10^{17}$ s$^{-1}$ |
| D | 0.25 | 0.43 | 0.95 | 1.39/1.49 | 6.5 | 18.0/9.1 | 0.44 | $1.29 \times 10^{17}$ s$^{-1}$ |

netic surface, respectively. The other parameters are the ion/electron temperature ratio $T_{\rm i}/T_{\rm e}$, the impurity density fractions $n_{\rm imp}/n_{\rm e}$ (normalised with the electron density), the safety factor $q$, the magnetic shear $\hat{s} = (r/q){\rm d}q/{\rm d}r$, the elongation $\kappa$, the triangularity $\delta$, the GENE collision parameter $\nu_{\rm c} = 2.3031 \times 10^{-5} \ln \Lambda R[{\rm m}] n_{\rm e}[10^{19}\ {\rm m}^{-3}]/T_{\rm e}[{\rm keV}]^2$, where $\ln \Lambda = 24 - \ln(\sqrt{10^{13} n_{\rm e}[10^{19}\ {\rm m}^{-3}]}/10^3 T_{\rm e}\ [{\rm keV}])$ is the Coulomb logarithm, the ratio of the electron plasma pressure to the magnetic pressure $\beta_{\rm e} = 2\mu_0 n_{\rm e} T_{\rm e}/B_0$, with $\mu_0$ the vacuum permeability and $B_0 = 5.9$ T the vacuum magnetic field on the magnetic axis. All simulations are run with collisions, using a Landau operator. Since the electron–ion collision rate depends on $n_{\rm i}$, which changes depending on the number of considered species ($n_{\rm i}$ is adapted using quasi-neutrality), the electron–ion thermal collision rate varies depending on the number of considered species and it can be easily evaluated for each case as $\nu_{\rm ei} = 4(n_{\rm i}/n_{\rm e})\sqrt{T_{\rm e}/m_{\rm e}}\nu_{\rm c}/R$. In the ASTRA-TGLF run the impurities have not been predicted; therefore, their density profiles are set proportional to the electron (ion) one. A realistic geometry has been considered, with magnetic equilibrium obtained with the EFIT solver [71, 72], then approximated with a Miller analytic model [73]. Fast ions have been excluded due to their small density fraction $n_{\rm FI}/n_{\rm e} \sim 2\%$ at the radius of analysis, but their potential effect on transport should be investigated in the future. Finally, the effect of the $E \times B$ rotation shear has been excluded ($\gamma_E = -(r/q)({\rm d}\Omega_{\rm tor}/{\rm d}r)R/c_{\rm s} = -0.03$, where $\Omega_{\rm tor}$ is the toroidal angular velocity and $c_{\rm s} \equiv \sqrt{T_{\rm e}/m_{\rm i}}$ the ion sound speed), since its effect has been found to be negligible by performing a NL GENE simulation at reference parameters.

To start, the linear $k_y$ spectra of the growth rate $\gamma$ and angular frequency $\omega$ corresponding to the first two most unstable modes have been computed with the GENE eigenvalue solver for reference parameters from the ASTRA-TGLF simulation at $\rho_{\rm tor} = 0.32$, in order to characterise the turbulence regime. The results are collected in figure 14.

The growth rate $\gamma$ (a) and the angular frequency $\omega$ (b) are shown versus $k_y$, comparing the simulations where the impurities have been excluded (black squares) with those where they have been taken into account (red triangles). $\gamma$ and $\omega$ are normalised with $c_{\rm s}/R$, while $k_y$ is normalised with $1/\rho_{\rm s}$, where $\rho_{\rm s} = c_{\rm s}/\Omega_{\rm i}$ is the sound Larmor radius, with $\Omega_{\rm i}$ the ion cyclotron frequency. The dominant mode is a TEM at all wavenumbers, while the second unstable mode is an ITG mode, corresponding to $\omega < 0$ and $\omega > 0$, respectively, according to GENE conventions. The sub-dominant ITGs are peaked at a larger wavenumber ($k_{y,\rm ITGpeak}\rho_{\rm s} \sim 0.6$) compared to the dominant TEMs ($k_{y,\rm TEMpeak}\rho_{\rm s} \sim 0.4$). As a consequence the ITGs are even more non-linearly sub-dominant, since smaller wavenumbers provide the dominant contribution to the NL fluxes. Micro tearing modes (MTM) are found with the GENE initial value solver for $k_y\rho_{\rm s} \leqslant 0.1$, which are destabilised by the finite $\beta_{\rm e}$ (they are identified as MTMs looking at the ballooning structures of the electrostatic potential fluctuation $\delta\phi$ and of the parallel vector potential fluctuation $\delta A_{\parallel}$). However, they correspond to small growth rates and do not impact the NL fluxes at the reference parameters. Finally, the impurities have a small stabilising effect on the smaller $k_y$ TEM branch, a moderate effect on the subdominant ITGs, while they considerably stabilise TEMs at $k_y\rho_{\rm s} > 0.8$, as seen when comparing the red and black curves in figure 15(*a*).

As a second step, a QL evaluation of the electron particle flux $\Gamma_{\rm e}$ spectrum dependence on $R/L_n$ has been pursued using a simple ES 'mixing length' model based on GENE linear simulations, following [74, 75]. For each $k_y$, the QL fluxes are evaluated as $F^{\rm QL} = A_0 \sum_{k_y} w^{\rm QL}(k_y) F^{\rm L}_{\rm norm}(k_y)$, where $A_0$ is a scaling factor associated with the absolute fluctuation amplitude, which is the same for different fluxes $F = \Gamma_{\rm e}, q_{\rm e}, q_{\rm i}$ and cancels out when computing flux ratios, $F^{\rm L}_{\rm norm}(k_y)$ represents a properly normalised spectral contribution to the flux which is evaluated with the fields from the corresponding linear eigenmode, and the QL saturation prescriptions $w^{\rm QL}(k_y) = (\gamma/\langle k_\perp^2\rangle)^\xi$ specify the $k_y$ dependence of the relative saturation amplitude levels of the NL electrostatic potential $\phi$. Here $\langle k_\perp^2\rangle$ indicates the flux-surface average of the squared perpendicular wave number, weighted with the $|\phi|^2$ ballooning structure, considering only $k_x = -\Delta k_x, 0, \Delta k_x$ ($\Delta k_x = 2\pi/L_x$, with $L_x$ the $x$ box size) following [76], and setting $\xi = 2$ (this, *a posteriori*, gives the best QL–NL spectra agreement). The QL results are summarised in figure 15.

Figure 15(*a*) shows the $\Gamma_{\rm e}$ spectrum, normalised with the total (summed over $k_y$) value of $(q_{\rm e} + q_{\rm i})/T_{\rm e}$, in the $(k_y\rho_{\rm s}, R/L_n)$ plane. The 'zero particle flux' condition $\Gamma_{\rm e} = 0$ (green line), which is very close to the actual $\Gamma_{\rm e} = \Gamma_{\rm e,ref.}$ from ASTRA-TGLF inputs ($\Gamma_{\rm e,ref.} \sim 1.01 \times 10^{18}$ s$^{-1}$ m$^{-2}$ at the radius of analysis and therefore almost negligible), is satisfied for $R/L_n \sim 1.8$, which is smaller than the TGLF SAT1-geo reference value $R/L_n \sim 3$ (magenta solid line), below a $\pm 30\%$ error bar. The $\Gamma_{\rm e} = 0$ condition is obtained from a balance of a low-$k$ TEM-driven outward flux with a larger-$k$ ITG-driven inward flux. This correspondence of the TEM and ITG regimes with the $\Gamma_{\rm e}$ signs is obtained by comparing figure 15(*a*) with figure 15(*b*), which shows the frequency $\omega$ in the $(k_y\rho_{\rm s}, R/L_n)$ plane ($> 0$ for ITG and $< 0$ for TEM according to GENE conventions).

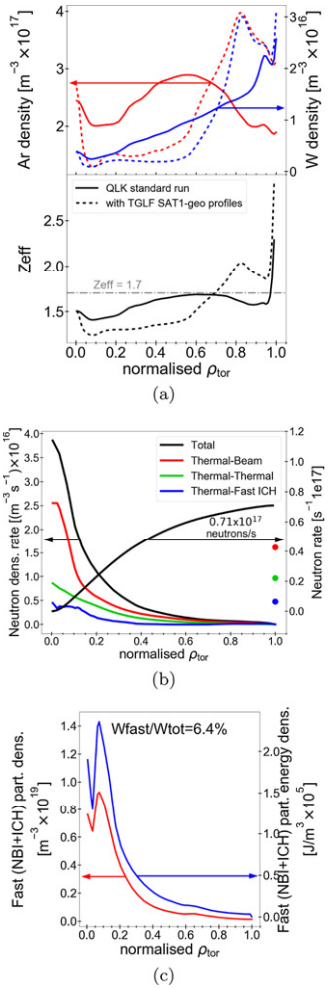


**Figure 20.** (*a*) Radial profiles of the impurity densities (Ar in red, W in blue) and of the effective charge in the day-1 scenario for the TGLF SAT1-geo case. The standard QLK case results (solid lines) are compared to an assessment of the impurity and $Z_{\rm eff}$ profiles in the presence of TGLF SAT1-geo-predicted profiles carried out with JETTO/SANCO and QLK (dashed lines). (*b*) Radial profiles of neutron density rates (neutrons from thermal nuclei in green, from a thermal nucleus and a fast NBI nucleus in red, and from a thermal nucleus and a fast ICRH nucleus in blue). The radial profile of the total neutron rate is also displayed (black). (*c*) Radial profiles of density and energy density of EPs due to the NBI and ICRH systems.

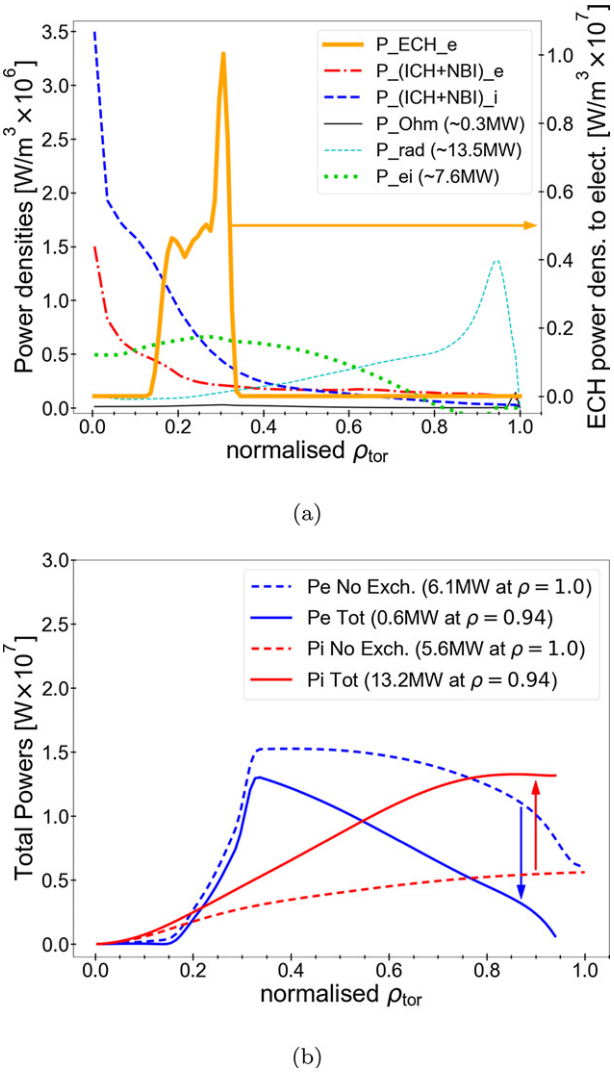


**Figure 21.** (*a*) Radial profiles of power densities in the day-1 scenario: ECRH power deposited to electrons $P_{\rm ECHe}$, NBI and ICRH power deposited to electrons $P_{\rm (ICH+NBI)e}$, NBI and ICRH power deposited to ions $P_{\rm (ICH+NBI)i}$, ohmic power $P_{\rm Ohm}$, radiative power $P_{\rm rad}$, and thermal exchange power between electrons and ions $P_{\rm ei}$. (*b*) Radial profiles of electron and ion total powers including or excluding the thermal exchange power between species in the day-1 scenario.

$R/L_n$ scans of NL GENE ion-scale local runs have been performed to obtain a GK estimate of the peaking (i.e. the $R/L_n$ that satisfies $\Gamma_{\rm e} \sim 0$). The GENE results are shown in figure 16 by solid black lines, compared with those obtained by running TGLF SAT1-geo (solid/red) and TGLF SAT2 (solid/blue) stand-alone simulations.

An additional $R/L_n$ scan of GENE NL runs (dashed/black) has been performed, replacing the values of the temperature logarithmic gradients $R/L_{T\rm e} = 7.8$, $R/L_{T\rm i} = 3.93$ (ASTRA-TGLF) with those corresponding to the JINTRAC-QLK predictive simulation: $R/L_{T\rm e} = 9.08$, $R/L_{T\rm i} = 4.58$, compared with corresponding QLK stand-alone simulations (dashed/green). The reference value of $R/L_n \sim 3$ from ASTRA-TGLF is shown by a solid vertical magenta line, while the corresponding value $R/L_n = 0.46$ from JINTRAC-QLK is shown by a dashed vertical magenta line. In greater detail, figure 16 shows the normalised electron particle flux $T_{\rm e}\Gamma_{\rm e}/(q_{\rm i} + q_{\rm e})$ vs $R/L_n$. The density peaking predicted by each code is obtained from figure 16(*a*) at the crossing of the corresponding curve with the horizontal line $\Gamma_{\rm e} \sim 0$. It follows that GENE prediction ($R/L_n \sim 1.4$–$1.8$) lies in between the QLK and TGLF presidctions, not confirming the 'flat $n_{\rm e}$' prediction of QLK. Even when replacing the ASTRA-TGLF $R/L_{T\rm e,i}$ values with those from JINTRAC-QLK, GENE still predicts a peaked $n_{\rm e}$, with an even slightly larger $R/L_n$.

The sensitivity of the GENE estimate of the electron density peaking to changes in $R/L_{T\rm e}$, which is the main driver of the TEM-dominant turbulence regime, has been tested by

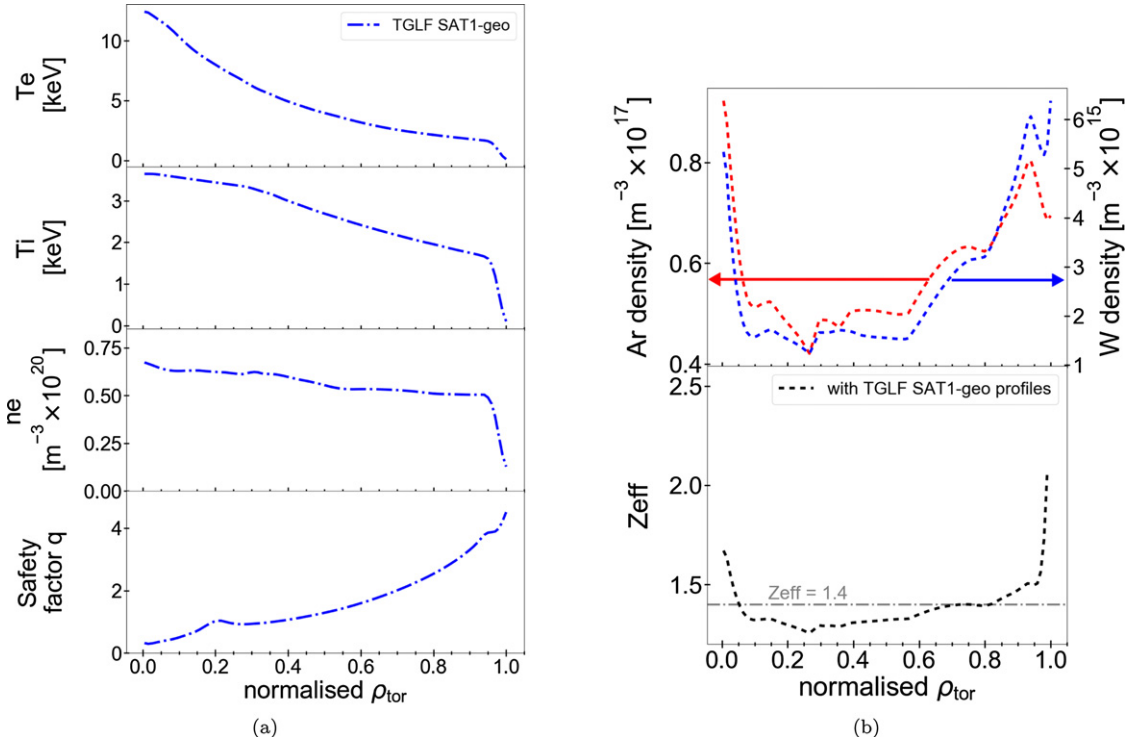


**Figure 22.** (*a*) Steady-state radial profiles of the electron and ion temperatures, electron density, and safety factor of the day-0 scenario, with turbulent transport calculated by TGLF SAT1-geo (blue dash-dotted line). (*b*) Radial profiles of the impurity densities (argon in red, tungsten in blue) and of the effective charge $Z_{\rm eff}$ in the day-0 scenario in the presence of TGLF SAT1-geo-predicted profiles carried out with JETTO/SANCO and QLK (dashed lines).

repeating the NL $R/L_n$ scans, increasing and decreasing the reference ASTRA-TGLF value $R/L_{T\rm e} = 7.8$ by $\pm 20\%$. The results, shown in figure 17, indicate that the effect of changing $R/L_{T\rm e}$ within a $\pm 20\%$ error bar has a small/moderate effect on the peaking, which increases by $\sim 20\%$ when $R/L_{T\rm e}$ decreases.

However, a similar sensitivity test in QLK indicated a significant increase in zero particle flux $R/L_{n\rm e}$ with decreasing $R/L_{T\rm e}$. Zero particle flux at $R/L_{n\rm e} = 1.5$ (the GENE value) was attained with only a $\sim$15% decrease in $R/L_{T\rm e}$. The zero-flux boundary in QLK is extremely sensitive to the ITG-TEM transition in this regime, and occurs here rapidly over multiple wavenumbers with stiff TEM heat flux, also meaning that the ad hoc TEM electron heat flux model tested here was less effective than expected in reducing the power balance $R/L_{T\rm e}$. The self-organized $R/L_n - R/L_T$ state that leads to flat $n_{\rm e}$ profiles in the QLK simulations for $\rho_{\rm tor} < 0.4$ in this specific regime thus likely arises from discrepancies in the ITG-TEM instability boundary in *the* $R/L_n - R/L_T$ space compared to higher-fidelity gyrokinetic models. This will be explored in future work.

Summing up, the very flat profile predicted by JINTRAC-QLK in the inner region is not validated by a comparison of QLK stand-alone with GENE. Also, the amount of $n_{\rm e}$ peaking predicted by ASTRA-TGLF turns out to be somewhat overestimated when compared with GENE, although qualitatively closer to the gyrokinetic prediction. Both models should then be approached with care in the region inside $\rho_{\rm tor} = 0.4$, which is characterised by high power density, TEM dominance and $q$ values below 1, with sawteeth not yet accounted for.

### 3.6. FP scenario heating mixes

Prior to this modelling work, the heating mix of the FP scenario was not established. One of the purposes of this work was to optimise the choice of power distribution amongst the three systems and the choice of NBI energy. In addition to the three heating mix options proposed in [6], other possible candidates have been suggested within the DTT physics group. The various options are listed in table 4.

In order to assist in the choice of heating mix, each of these nine SN FP H-mode scenarios has been simulated both in a JETTO run with the standard QLK model and with a JINTRAC-ASTRA approach with TGLF SAT1-geo model.

For the sake of clarity, only some radial profiles of only the three most salient options obtained from TGLF SAT1-geo runs are shown in figure 18. The main parameters of these three cases are displayed in table 5. In all FP options, the characteristic behaviour of the main plasma profiles seen in section 3.5.1 recurs. Of particular note, the electron density has a moderately peaked profile reaching maximum values in the range of (1.9–2.7) $\times$ $10^{20}$ m$^{-3}$, and in the central plasma region the electron temperature $T_{\rm e} \approx 15$–27 keV is much higher than the ion temperature $T_{\rm i} \approx 8$–12 keV.

In order to achieve more central NBI deposition, as well as to minimise the collisionless ripple fast particle losses [77] and allow resonant excitation of Alfvénic waves [78],

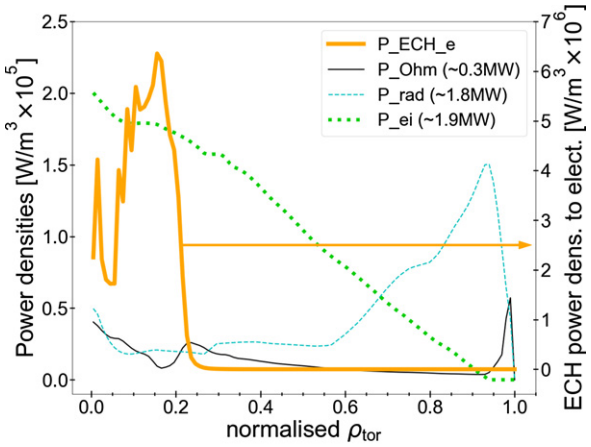


(a)

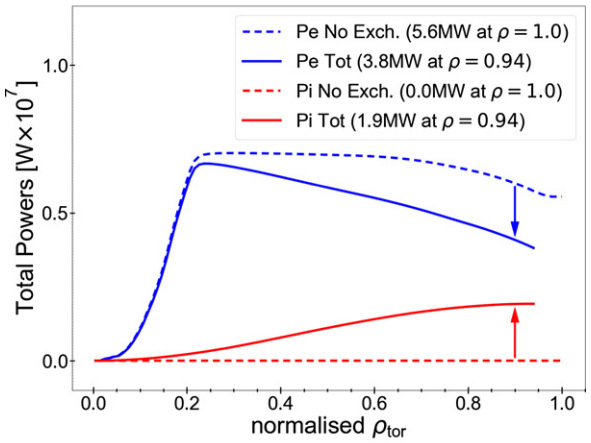


(b)

**Figure 23.** (*a*) Radial profiles of the power densities in the day-0 scenario: ECRH power deposited to electrons $P_{\mathrm{ECHe}}$, ohmic power $P_{\mathrm{Ohm}}$, radiative power $P_{\mathrm{rad}}$, and thermal exchange power between electrons and ions $P_{\mathrm{ei}}$. (*b*) Radial profiles of electron and ion total powers including or excluding the thermal exchange power between species in the day-0 scenario.

the higher NBI energy is preferred over the higher NBI power option, in addition to opting for the largest possible injection angle.

Given the need to try to equilibrate $T_{\mathrm{e}}$ and $T_{\mathrm{i}}$, option B with 40 MW of ECH power has been discarded, and the missing NBI power has been replaced by ICH power, which has the double advantage of providing central ion heating and a fast particle population, which could help lowerthe high ion stiffness observed by TGLF and QLK [59]. From the power deposition calculations, the synergy effects between ICRH and NBI proved to be very relevant, leading to a maximised energetic particle content in option D.

Given the state of the art of QL models, the differences between the various options are not large. However, the nonlinear effects linked with thermal and suprathermal pressure gradients not included in the QL models could play an important role in the ion temperature profile.

From the physics point of view, option D is the best compromise between technical feasibility, the need to heat ions, and the creation of suitable EP population.

### 3.7. Day 1 scenario

In the day-1 phase (with $B_{\mathrm{t}} = 6$ T and $I_{\mathrm{pl}} = 4.0$ MA), the power coupled to the plasma (~25 MW) will be shared among the heating systems as described in section 2. The integrated modelling of a steady-state deuterium plasma in the day-1 scenario has been performed using both the standard QLK model in a JETTO run and the TGLF SAT1-geo model with the JINTRAC-ASTRA approach.

The simulation settings broadly described from the beginning of section 3.1 up to the end of section 3.4 have been also employed in this day-1 scenario modelling work.

Since the density value at the top of the pedestal has not been reduced with respect to the FP case, the Greenwald fraction increased to $\langle ne \rangle \sim 0.5\, n_{\mathrm{G}}$, still well within safety margins. The pedestal parameters predicted by Europed for day-1 scenario are very similar to those of the FP case.

The electron temperature $T_{\mathrm{e}}$, ion temperature $T_{\mathrm{i}}$, electron density $n_{\mathrm{e}}$, toroidal rotation $\omega_{\mathrm{tor}}$, and safety factor $q$ radial profiles obtained by TGLF SAT1-geo and QLK runs are displayed in figure 19. According to both models, the density peaking results were less pronounced in day-1 phase than in the reference FP scenario, leading to a lower central value $n_{\mathrm{e}_0} \approx 2.0 \times 10^{20}$ m$^{-3}$.

We note some discrepancies between the QLK and TGLF temperature profiles. In the day-1 case, the electron temperature in the QLK run is estimated to be rather similar to the FP case, while it is significantly reduced in the TGLF run. For both models, the $T_{\mathrm{i}}$ values are similar in the day-1 and FP scenarios, in spite of having half the injected power. This may be ascribed both to the increased ITG threshold with lower $T_{\mathrm{e}}/T_{\mathrm{i}}$ and to the high ion stiffness, which makes a factor of 2 difference in power rather ineffective in terms of $T_{\mathrm{i}}$ profiles (although crucial for divertor studies).

Figure 20(*a*) shows impurity densities and effective charge radial profiles for the standard QLK run (solid lines) compared to an assessment of the impurity and $Z_{\mathrm{eff}}$ profiles in the presence of TGLF SAT1-geo predicted profiles carried out with JETTO/SANCO and QLK (dashed lines). We note that the impurities feature less central accumulation than in the FP case.

For the TGLF case, shown in figure 20(*b*), the neutron rate is reduced to $7.1 \times 10^{16}$ neutrons s$^{-1}$. In figure 20(*c*) the EP contents are shown for the TGLF SAT1-geo case.

In figure 21(*a*) the radial profiles of all power densities and those of the total electron and ion powers are shown in figure 21(*b*), only for the standard QLK simulation.

### 3.8. Day 0 scenario

The day-0 phase (with $B_{\mathrm{t}} = 3$ T and $I_{\mathrm{pl}} = 2.0$ MA) features only 8 MW of ECH power in second harmonic X-mode (coupling to the plasma ~7.2 MW of power), as described in section 2. The integrated modelling of a steady-state deuterium plasma in the day-0 scenario has been performed using the TGLF SAT1-geo

model with the JINTRAC-ASTRA approach. We do not show the QLK results for this case, as QLK validity is most affected by the dominant TEM regime in this purely electron heated case.

The simulation settings widely described in the initial sections of 3 have also been used in this day-0 scenario modelling work. While maintaining the same relative impurity mix of Ar and W used in the FP runs, in the day-0 simulation a flat $Z_{\mathrm{eff}} = 1.4$ profile has been set as the initial condition in SANCO. The density at the pedestal top has been reduced with respect to the FP case, to have a Greenwald fraction of approximately 0.36.

In figure 22(*a*), the radial profiles of $T_{\mathrm{e}}$, $T_{\mathrm{i}}$, $n_{\mathrm{e}}$, and $q$ predicted by the TGLF SAT1-geo run of day-0 phase are shown. The reduced pedestal density with respect to the FP case and the slightly peaked $n_{\mathrm{e}}$ profile lead to a lower central density value of about $n_{\mathrm{e}_0} \approx 0.7 \times 10^{20}$ m$^{-3}$.

In figure 22(*b*), impurity densities and effective charge radial profiles are shown for an assessment of the impurity and $Z_{\mathrm{eff}}$ profiles in the presence of TGLF SAT1-geo-predicted profiles carried out with JETTO/SANCO and QLK (dashed lines). $T_{\mathrm{e}}$ is much larger that $T_{\mathrm{i}}$ ($T_{\mathrm{e}_0} \approx 12$ keV and $T_{\mathrm{i}_0} \approx 4$ keV), due to having only electron heating and low density. The toroidal rotation is not shown as there is no NBI torque, so it reduces to intrinsic rotation, with edge values difficult to estimate but which are expected to be small. We note that the impurities show much less core penetration in the day-0 case.

For the sake of completeness, in figure 21 the radial profiles of all power densities and those of the total electron and ion powers are shown in figures 23(*a*) and (*b*), respectively.

A neutron rate of $\sim 4 \times 10^{14}$ neutrons s$^{-1}$ has been estimated for the day-0 scenario.

## 4. Conclusions

The first principle multi-channel-integrated modelling of the main DTT baseline scenarios using QL transport models (TGLF, QLK) has begun and it is key to supporting the design of the device and to help the elaboration of a scientific work programme for DDT. This work has been partiuclarly crucial for defining the reference heating mix for the FP scenario among nine possible options. Moreover, results from this modelling led to the decision to enlarge the device up to $R_0 = 2.19$ m and $a = 0.70$ m. Reference profiles in different scenarios, as well as estimates of neutron yields and fast particle losses, are now available for diagnostic system design. In addition, a preliminary risk evaluation of fuelling via gas puffing without pellet support has been done, suggesting a beneficial impact of incorporating pellet fuelling in addition to gas puffing. Validation of the QL models used against the gyrokinetic simulations in the specific DTT range of parameters has been performed, essential to improve the reliability of such predictions.

## Acknowledgments

This work has been carried out in the framework of the DTT design. The authors are very grateful to all colleagues involved in the DTT project for their essential contributions. We thank G. Tardini for providing help with the simulations using ASTRA code. We thank G.M. Staebler for providing advice on the use of the TGLF model and T. Goerler for advice on the GENE simulations. This work was partially funded by the RCUK Energy Programme (Grant No. EP/T012250/1). The first author has worked under a PhD grant financed by ENEA.

## ORCID iDs

I. Casiraghi https://orcid.org/0000-0002-1719-6682
P. Mantica https://orcid.org/0000-0001-5939-5244
R. Ambrosino https://orcid.org/0000-0001-8799-5837
J. Citrin https://orcid.org/0000-0001-8007-5501
L. Frassinetti https://orcid.org/0000-0002-9546-4494
A. Mariani https://orcid.org/0000-0003-0476-3825
P. Vincenzi https://orcid.org/0000-0002-5156-4354
P. Agostinetti https://orcid.org/0000-0003-2103-7630
L. Balbinot https://orcid.org/0000-0002-7467-533X
S. Ceccuzzi https://orcid.org/0000-0003-1448-5793
L. Figini https://orcid.org/0000-0002-0034-4028
G. Granucci https://orcid.org/0000-0002-6958-7028
P. Innocente https://orcid.org/0000-0001-8726-994X
T. Johnson https://orcid.org/0000-0002-7142-7103
H. Nyström https://orcid.org/0000-0002-1310-4517

## References

[1] EFDA 2012 Fusion electricity—a roadmap to the realisation of fusion energy (https://euro-fusion.org/fileadmin/user_upload/Archive/wp-content/uploads/2013/01/JG12.356-web.pdf)
[2] EUROfusion 2018 European research roadmap to the realisation of fusion energy (https://euro-fusion.org/fileadmin/user_upload/EUROfusion/Documents/2018_Research_roadmap_long_version_01.pdf)
[3] https://iter.org/
[4] https://euro-fusion.org/programme/demo/
[5] Granucci G. *et al* 2017 *Fusion Eng. Des.* **122** 349–55
[6] Martone R., Albanese R., Crisanti F., Martin P. and Pizzuto A. (ed) 2019 *Divertor Tokamak Test Facility: Interim Design Report (Green Book), ENEA Internal Report* (ENEA Frascati Research Center)
[7] https://dtt-project.enea.it/
[8] Pizzuto A. *et al* 2010 *Nucl. Fusion* **50** 095005
[9] Thomas D.M., Leonard A.W., Osborne T.H., Groebner R.J., West W.P. and Burrell K.H. 2006 *Plasma Phys. Control. Fusion* **48** A183
[10] ITER Organization 2018 ITER research plan within the staged approach (level III—provisional version) *Report ITR-18-003* (ITER Organization)
[11] Kukushkin A.S., Pacher H.D., Pacher G.W., Janeschitz G., Coster D., Loarte A. and Reiter D. 2003 *Nucl. Fusion* **43** 716
[12] Wenninger R. *et al* 2017 *Nucl. Fusion* **57** 016011

[13] Greenwald M. 2002 *Plasma Phys. Control. Fusion* **44** R27
[14] Romanelli M. *et al* 2014 *Plasma Fusion Res.* **9** 3403023
[15] Pereverzev G.V. and Yushmanov P.N. 2002 ASTRA automated system for transport analysis in a tokamak *IPP Report 5/98* Max-Planck-Institut für Plasmaphysik
[16] Saarelma S., Challis C.D., Garzotti L., Frassinetti L., Maggi C.F., Romanelli M. and Stokes C. 2018 *Plasma Phys. Control. Fusion* **60** 014042
[17] Snyder P.B., Groebner R.J., Hughes J.W., Osborne T.H., Beurskens M., Leonard A.W., Wilson H.R. and Xu X.Q. 2011 *Nucl. Fusion* **51** 103016
[18] Stefanikova E. *et al* 2018 *Nucl. Fusion* **58** 056010
[19] Frassinetti L. *et al* 2021 *Nucl. Fusion* **61** 016001
[20] Staebler G.M., Candy J., Howard N.T. and Holland C. 2016 *Phys. Plasmas* **23** 062518
[21] Kinsey J.E., Staebler G.M. and Waltz R.E. 2008 *Phys. Plasmas* **15** 055908
[22] Staebler G.M., Kinsey J.E. and Waltz R.E. 2007 *Phys. Plasmas* **14** 055909
[23] Staebler G.M., Kinsey J.E. and Waltz R.E. 2005 *Phys. Plasmas* **12** 102508
[24] Citrin J. *et al* 2017 *Plasma Phys. Control. Fusion* **59** 124005
[25] Bourdelle C., Citrin J., Baiocchi B., Casati A., Cottier P., Garbet X. and Imbeaux F. 2016 *Plasma Phys. Control. Fusion* **58** 014036
[26] Mantica P., Angioni C., Bonanomi N., Citrin J., Grierson B.A., Koechl F., Mariani A. and Staebler G.M. 2020 *Plasma Phys. Control. Fusion* **62** 014021
[27] Mordijck S. *et al* 2020 *Nucl. Fusion* **60** 066019
[28] Grierson B.A., Staebler G.M., Solomon W.M., McKee G.R., Holland C., Austin M., Marinoni A., Schmitz L. and Pinsker R.I. 2018 *Phys. Plasmas* **25** 022509
[29] Doyle E.J. *et al* (FEC) 2012 *IAEA Fusion Energy Conf. EX/P3-26*
[30] Angioni C., Fable E., Ryter F., Rodriguez-Fernandez P. and Pütterich T. 2019 *Nucl. Fusion* **59** 106007
[31] Ho A., Citrin J., Auriemma F., Bourdelle C., Casson F.J., Kim H.-T., Manas P., Szepesi G. and Weisen H. 2019 *Nucl. Fusion* **59** 056007
[32] Marin M., Citrin J., Bourdelle C., Camenen Y., Casson F.J., Ho A., Koechl F. and Maslov M. 2020 *Nucl. Fusion* **60** 046007
[33] Marin M. *et al* (JET Contributors) 2021 *Nucl. Fusion* **61** 036042
[34] Casson F.J. *et al* 2020 *Nucl. Fusion* **60** 066029
[35] Kiefer C.K., Angioni C., Tardini G., Bonanomi N., Geiger B., Mantica P., Pütterich T., Fable E. and Schneider P.A. 2021 *Nucl. Fusion* **61** 066035
[36] Staebler G.M., Candy J., Belli E.A., Kinsey J.E., Bonanomi N. and Patel B. 2021 *Plasma Phys. Control. Fusion* **63** 015013
[37] Stephens C. et al Phys. Plasmas (submitted)
[38] van de Plassche K.L., Citrin J., Bourdelle C., Camenen Y., Casson F.J., Dagnelie V.I., Felici F., Ho A. and Van Mulders S. 2020 *Phys. Plasmas* **27** 022310
[39] Romanelli M. and Ottaviani M. 1998 *Plasma Phys. Control. Fusion* **40** 1767
[40] Houlberg W.A., Shaing K.C., Hirshman S.P. and Zarnstorff M.C. 1997 *Phys. Plasmas* **4** 3230–42
[41] Peeters A.G., Angioni C., Camenen Y., Casson F.J., Hornsby W.A., Snodin A.P. and Strintzi D. 2009 *Phys. Plasmas* **16** 062311
[42] Peeters A.G. *et al* 2011 *Nucl. Fusion* **51** 094027
[43] Taroni L. 1994 *21st EPS Conf. Contr Fus Plas Phys—Montpellier* 102 I
[44] Cenacchi G. and Taroni A. 1988 *ENEA-RT-TIB 88-5* ENEA
[45] Ivanov A.A. 2005 *32nd EPS Conf. on Plasma Physics—Terragona 29C (ECA)* P-5.063
[46] Albanese R., Ambrosino R. and Mattei M. 2015 *Fusion Eng. Des.* **96-97** 664–7
[47] Farina D. 2007 *Fusion Sci. Technol.* **52** 154 –60
[48] Challis C.D., Cordey J.G., Hamnén H., Stubberfield P.M., Christiansen J.P., Lazzaro E., Muir D.G., Stork D. and Thompson E. 1989 *Nucl. Fusion* **29** 563
[49] Agostinetti P., Bolzonella T., Gobbin M., Sonato P., Spizzo G., Vallar M. and Vincenzi P. 2019 *Fusion Eng. Des.* **146** 441–6
[50] Eriksson L.-G., Hellsten T. and Willen U. 1993 *Nucl. Fusion* **33** 1037
[51] Hellsten T. and Eriksson L.-G. 1989 *Nucl. Fusion* **29** 2165
[52] Hellsten T. and Villard L. 1988 *Nucl. Fusion* **28** 285
[53] Görler T., Lapillonne X., Brunner S., Dannert T., Jenko F., Merz F. and Told D. 2011 *J. Comput. Phys.* **230** 7053–71
[54] http://genecode.org/
[55] Romanelli F. and Zonca F. 1993 *Phys. Fluids* B **5** 4081–9
[56] Romanelli F. 1989 *Phys. Fluids* B **1** 1018–25
[57] Beurskens M. *et al* (IAEA FEC) 2020 *IAEA-CN-EX/6-3* International Atomic Energy Agency
[58] Jenko F., Dorland W. and Hammett G.W. 2001 *Phys. Plasmas* **8** 4096–104
[59] Di Siena A., Görler T., Doerk H., Poli E. and Bilato R. 2018 *Nucl. Fusion* **58** 054002
[60] Di Siena A., Görler T., Poli E., Navarro A.B., Biancalani A. and Jenko F. 2019 *Nucl. Fusion* **59** 124001
[61] Garofalo A.M. *et al* 2014 *Fusion Eng. Des.* **89** 876–81
[62] Dunne M.G. *et al* 2017 *Plasma Phys. Control. Fusion* **59** 025010
[63] Frassinetti L. *et al* 2019 *Nucl. Fusion* **59** 076038
[64] Sheikh U.A. *et al* 2019 *Plasma Phys. Control. Fusion* **61** 014002
[65] Wang H.Q. *et al* 2018 *Nucl. Fusion* **58** 096014
[66] Frassinetti L. 2020 *IAEA Fusion Energy Conf. (FEC 2020)* EX/2-2 28th
[67] Tamor S. 1981 *J. Comput. Phys.* **40** 104
[68] Balbinot L., Rubino G. and Innocente P. 2021 *Nucl. Mater. Energy* **27** 100952
[69] Bufferand H. *et al* 2013 *J. Nucl. Mater.* **438** 445S–8
[70] Bufferand H. *et al* 2015 *Nucl. Fusion* **55** 053025
[71] Lao L.L., St. John H., Stambaugh R.D., Kellman A.G. and Pfeiffer W. 1985 *Nucl. Fusion* **25** 1611
[72] Brix M., Hawkes N.C., Boboc A., Drozdov V. and Sharapov S.E. 2008 *Rev. Sci. Instrum.* **79** 10F325
[73] Miller R.L., Chu M.S., Greene J.M., Lin-Liu Y.R. and Waltz R.E. 1998 *Phys. Plasmas* **5** 973
[74] Mariani A., Brunner S., Dominski J., Merle A., Merlo G., Sauter O., Görler T., Jenko F. and Told D. 2018 *Phys. Plasmas* **25** 012313
[75] Mariani A., Brunner S., Merlo G. and Sauter O. 2019 *Plasma Phys. Control. Fusion* **61** 064005
[76] Jenko F., Dannert T. and Angioni C. 2005 *Plasma Phys. Control. Fusion* **47** B195
[77] Spizzo G. 2021 *Nucl. Fusion* (https://doi.org/10.1088/1741-4326/ac1e08)
[78] Chen L. and Zonca F. 2016 *Rev. Mod. Phys.* **88** 015008